

1 **Regulation of sedimentation rate shapes the evolution of multicellularity in a unicellular**  
2 **relative of animals.**

3 Omayá Dudin<sup>1†</sup>, Sébastien Wielgoss<sup>2</sup>, Aaron M. New<sup>3</sup>, Iñaki Ruiz-Trillo<sup>1,4,5</sup>

4

5 <sup>1</sup>Institut de Biologia Evolutiva (CSIC-Universitat Pompeu Fabra), Passeig 12 Marítim de la  
6 Barceloneta 37-49, 08003 Barcelona, Catalonia, Spain

7 <sup>2</sup>Institute of Integrative Biology, Department of Environmental Systems Science, ETH Zürich,  
8 Zürich, Switzerland

9 <sup>3</sup>Centre for Genomic Regulation (CRG), The Barcelona Institute for Science and Technology,  
10 Dr. Aiguader 88, 08003, Barcelona, Spain

11 <sup>4</sup>Departament de Genètica, Microbiologia i Estadística, Universitat de Barcelona, Av.  
12 Diagonal, 645, 08028 Barcelona, Catalonia, Spain

13 <sup>5</sup>ICREA, Passeig Lluís Companys 23, 08010, Barcelona, Catalonia, Spain

14 † Present address: Swiss Institute for Experimental Cancer Research, School of Life Sciences,  
15 Swiss Federal Institute of Technology (EPFL), 1015 Lausanne, Switzerland

16 \* Lead Contact: [omaya.dudin@epfl.ch](mailto:omaya.dudin@epfl.ch)

17 **Abstract**

18

19 Significant increases in sedimentation rate accompany the evolution of multicellularity. These  
20 increases should lead to rapid changes in ecological distribution, thereby affecting the costs  
21 and benefits of multicellularity and its likelihood to evolve. However, how genetic and cellular  
22 traits which control this process, their likelihood of emergence over evolutionary timescales,  
23 and the variation in these traits as multicellularity evolves, are still poorly understood. Here,  
24 using isolates of the ichthyosporean *Sphaeroforma* genus - close unicellular relatives of  
25 animals with brief transient multicellular life stages - we demonstrate that sedimentation rate  
26 is a highly variable and evolvable trait affected by at least two distinct physical mechanisms.  
27 We first find a dramatic >300x variation in sedimentation rate for different *Sphaeroforma*  
28 species, mainly driven by size and density during the unicellular-to-multicellular life cycle  
29 transition. Using experimental evolution with sedimentation rate as a focal trait, we readily  
30 obtained fast settling *S. arctica* isolates. Quantitative microscopy showed that increased  
31 sedimentation rates most often arose by incomplete cellular separation after cell division,  
32 leading to clonal “clumping” multicellular variants with increased size and density. Additionally,  
33 density increases arose by an acceleration of the nuclear doubling time relative to cell size.  
34 Similar size- and density-affecting phenotypes were observed in four additional species from  
35 the *Sphaeroforma* genus, suggesting variation in these traits might be widespread in the  
36 marine habitat. By sequencing evolved isolates, we identified mutations in regulators of  
37 cytokinesis, plasma membrane remodelling, and chromatin condensation that may contribute  
38 to both clump formation and the increase in the nuclear number-to-volume ratio. Taken  
39 together, this study illustrates how extensive cellular control of density and size drive  
40 sedimentation rate variation, likely shaping the evolution of multicellularity.

## 41 Introduction

42

43 The emergence of multicellularity from single-celled life represents a major transition which  
44 has occurred many times independently across the tree of life (Grosberg & Strathmann, 2007;  
45 Knoll, 2011; Leigh et al., 1995; Niklas & Newman, 2013; Parfrey & Lahr, 2013; Rokas, 2008;  
46 Ruiz-Trillo et al., 2007; Sebé-Pedrós et al., 2017). Multicellularity can arise either by  
47 aggregation of single cells that come together, or from single cells that are maintained together  
48 clonally after division (Bonner, 1998; Tarnita et al., 2013; Wielgoss et al., 2019). The unicellular  
49 and intermediate multicellular ancestors which led to present-day multicellular organisms have  
50 long been extinct (Grosberg & Strathmann, 2007), obscuring direct investigation of how  
51 multicellular life has emerged. However, several strategies have been used to study the  
52 emergence of multicellularity, including the use of experimental evolution (EE) approaches  
53 and the investigation of novel non-model organisms at pivotal positions in the tree of life.

54 For example, EE under controlled conditions allows selection for diverse phenotypes (Elena  
55 & Lenski, 2003; Kawecki et al., 2012), including multicellularity (Herron et al., 2019;  
56 Koschwanez et al., 2013; Ratcliff et al., 2012, 2013, 2015). Using EE, Ratcliff and colleagues  
57 repeatedly observed the evolution of a simple form of multicellularity in *Saccharomyces*  
58 *cerevisiae* and *Chlamydomonas reinhardtii* in response to gravitational selection (Oud et al.,  
59 2013; Ratcliff et al., 2012, 2013, 2015). Similarly, multicellularity emerged in yeast as a  
60 mechanism to improve the use of public goods (Koschwanez et al., 2013). In all these cases,  
61 cells form clumps by incomplete separation of daughters from mother cells, instead of by post-  
62 mitotic aggregation (Fisher et al., 2013; Queller et al., 2003; Strassmann et al., 2011).

63 Alternatively, non-model organisms with key evolutionary positions can be used to better  
64 understand the emergence of multicellularity. In particular, the study of unicellular holozoans  
65 (Figure 1A), the closest unicellular relatives of animals, revealed that these organisms contain  
66 a rich repertoire of genes required for cell-adhesion, cell signalling and transcriptional  
67 regulation, and that each unicellular holozoan lineage uses a distinct developmental mode  
68 that includes transient multicellular forms (Brunet et al., 2019; Brunet & King, 2017; Parra-  
69 Acero et al., 2020; Pérez-Posada et al., 2020; Ruiz-Trillo & de Mendoza, 2020; Sebé-Pedrós  
70 et al., 2017). For instance, the choanoflagellate *Salpingoeca rosetta* can form clonal  
71 multicellular colonies through serial cell division in response to a bacterial sulphonolipid  
72 (Alegado et al., 2012; Fairclough et al., 2010; Levin et al., 2014), whereas the filasterean  
73 *Capsaspora owczarzaki* can form multicellular structures by aggregation (Sebé-Pedrós et al.,  
74 2013). Ichthyosporeans display a coenocytic life cycle unique among unicellular holozoan  
75 lineages and pass through a short and transient clonal multicellular life-stage prior to the

76 release of new-born cells (A. de Mendoza et al., 2015; Dudin et al., 2019; Glockling et al.,  
77 2013; L. Mendoza et al., 2002; Ondracka et al., 2018).

78 Alongside the formation of new biological structures and increases in size, the emergence of  
79 multicellularity is invariably accompanied with an increase in sedimentation rate. Indeed,  
80 snowflake yeasts, multicellular *C. reinhardtii* and *S. rosetta* colonies sediment faster when  
81 compared to their unicellular counterparts (Ratcliff et al., 2012, 2013; Thibaut Brunet –  
82 Personal communication). Such correlation has been described in several marine  
83 phytoplankton species where multicellular life-stages show faster-sedimentation than  
84 unicellular ones (Beardall et al., 2009; Eppley et al., 1967; Finkel et al., 2010; Smayda, 1971).  
85 This phenotype has a large impact on where in the water column these microbes proliferate  
86 (Beardall et al., 2009; Friebele et al., 1978; Gemmell et al., 2016; N. B. Marshall, 1954), and  
87 thus is presumed to be under strong genetic control and selective pressure. Despite its  
88 capacity to affect the depth at which marine species flourish, the role of sedimentation rate,  
89 the potential impact of its variation and its connection to the emergence of multicellularity has  
90 not been systematically analysed across unicellular marine organisms, including in the closest  
91 unicellular relatives of animals with transient multicellular life-stages. Here, we characterize  
92 how regulation of sedimentation rate can influence emergence of multicellular life-forms in the  
93 ichthyosporean *Sphaeroforma* genus, a close unicellular relative of animals.

## 94 **Results**

95

### 96 ***Sphaeroforma* species exhibit large variation in sedimentation rates**

97 Similar to other ichthyosporean species, *Sphaeroforma* species proliferate through continuous  
98 rounds of nuclear divisions without cytokinesis to form a multinucleated coenocyte (Glockling  
99 et al., 2013; W. L. Marshall et al., 2008; Ondracka et al., 2018; Suga & Ruiz-Trillo, 2013).  
100 *Sphaeroforma* coenocytes then undergo a coordinated cellularization process leading to the  
101 formation of a transient multicellular life-stage resembling an epithelium (Dudin et al., 2019).  
102 This layer of cells then detaches and cell-walled new-born cells are released to the  
103 environment (Figure 1B) (Dudin et al., 2019). The entire life cycle prior to cellularization occurs  
104 in highly spherical (multinucleated) cells.

105 Extensive literature has documented a positive correlation between cell size and  
106 sedimentation rate, including during the life cycle of marine phytoplankton (Figure 1C)  
107 (SMAYDA & J., 1970; Smayda, 1971). This is consistent with Stoke's law, which shows that  
108 the relationship between a spherical particle's terminal sedimentation rate  $v$  in a fluid and its  
109 radius  $R$  should be determined by

$$110 \quad v = c p_p R^2$$

111 Where  $c$  represents the scaled ratio of gravitational to viscosity constants, and  $p_p$  is the  
112 difference between the particle's and the fluid's densities (see Methods). Therefore, even  
113 small shifts in a particle's radius will lead to pronounced (i.e., quadratic) changes in  
114 sedimentation rate. Similarly, for particles sitting near the buoyancy threshold, small changes  
115 in density can lead to proportionally large changes in settling rate (Figure 1D).

116 Due to the nature of the coenocytic life cycle (Figure 1B), which is associated with an increase  
117 in the number of nuclei and coenocyte volume, we expected to observe an increase in cellular  
118 sedimentation rates over time (Allen, 1932; N. B. Marshall, 1954; Waite et al., 1997). To better  
119 understand this relationship, throughout this study, we conducted overlapping experiments  
120 characterizing cell volume and sedimentation rates of *Sphaeroforma* species for cultures  
121 growing at 17°C for 72 hours. For certain replicates of this core dataset, we included  
122 measurements of various genetic variants, the temperature dependence of phenotypes, as  
123 well as the speed of nuclear duplication. Overall, the measurements we report are highly  
124 reproducible with >95% variance explained for replicate measurements across phenotypes  
125 (Figure 1- data source 1 – 3) (see Methods).

126 To begin, we measured the sedimentation rate of five different *Sphaeroforma* species that  
127 have been isolated either free-living or derived from different marine hosts: *S. arctica*, *S.*  
128 *sirkka*, *S. napiecek*, *S. gastrica* and *S. nootakensis* using a quantitative sedimentation rate  
129 assay based on changes in optical density over time (Ducluzeau et al., 2018; Dudin et al.,  
130 2019; Hassett et al., 2015; Jøstensen et al., 2002; W. L. Marshall et al., 2008; W. L. Marshall  
131 & Berbee, 2013). According to these estimates, cell sedimentation rates varied greatly, from  
132 between 0.4 to 125  $\mu\text{m}$  per second (i.e., up to 0.45 meters per day) (Figure 1E). This broad  
133 variability over the life cycle and among *Sphaeroforma* species suggested that appreciable  
134 changes in size and/or cellular density should accompany different stages of the life cycle.

### 135 **The transient multicellular life stage of *S. arctica* is associated with an increase in** 136 **sedimentation rate**

137 To better understand the cellular basis of sedimentation rate variation, we focused on *S.*  
138 *arctica*, the most studied *Sphaeroforma* species to date (Dudin et al., 2019; Jøstensen et al.,  
139 2002; Ondracka et al., 2018). Using fixed-cell imaging, we observed that synchronized  
140 cultures of *S. arctica* undergo a complete life cycle in about 48 hours and can reach up to 256  
141 nuclei per coenocyte before undergoing cellularization and releasing new-born cells (Figure  
142 1F). Prior to this release, all cellular division occurs in highly spherical mother coenocytes.  
143 Consistent with previous results (Ondracka et al., 2018), nuclear division cycles were periodic  
144 during coenocytic growth and occurred on average every 9-10 hours, as measured indirectly  
145 from changes in DNA content (Figure 1G). Average cell volume increased throughout the

146 coenocytic cycle to reach its maximum value at 36 hours prior to the release of new-born cells  
147 (Figure 1H). Similarly, the sedimentation rate increased up to >300-fold the initial value after  
148 36 hours (Figure 1I). Altogether, we observe that every cycle of nuclear division is associated  
149 with a significant increase in nuclear content, volume and sedimentation rate with a distinct  
150 peak reached before cell release. As the transient multicellular life-stage of *S. arctica* occurs  
151 during the latest stages of cellularization and ahead of cell-release (Dudin et al., 2019), our  
152 results suggest that it is tightly associated with an increased sedimentation rate.

### 153 **Experimental evolution of fast-settling mutants**

154 Given how cell size and division across the cell cycle are regulated, we reasoned that these  
155 variable traits should also be heritable and hence evolvable. To test this, we conducted an  
156 evolution experiment to generate mutants with increased sedimentation rates (Herron et al.,  
157 2019; Ratcliff et al., 2012, 2013). Briefly, 10 independent cultures of *S. arctica* (S1 to S10)  
158 originating from the same ancestral clone (AN) (Figure 2A), were diluted in fresh marine broth  
159 medium at 17°C (Figure 1C). Selection was performed every 24 hours by allowing the cultures  
160 to sediment in tubes for 2 minutes before transferring and propagating the fastest-settling cells  
161 in fresh medium (Figure 2A). Experimental evolution was continued for 56 transfers (8 weeks)  
162 or about 364 nuclear generations and a frozen fossil was conserved every 7 transfers (1 week)  
163 (see Methods) (Figure 2—figure supplement 1A, Figure 2- Source data 1).

164 To determine the timing of when this phenotype arose, we revived evolved population isolates  
165 (lineages) from the freezer. Most lineages exhibited a distinct clumping phenotype to varying  
166 degrees across all evolved populations (Figure 2B). The clumps of cells were not maintained  
167 by ionic forces or protein-dependent interactions, however could be separated by mild  
168 sonication without leading to cell lysis (Figure 2- figure supplement 1B). To assess when  
169 sedimentation rates increased during the selection process for each evolved population, we  
170 synchronized cultures using mild sonication before dilution in fresh medium and allowed them  
171 to undergo a complete life cycle before measuring the sedimentation rate (Figure 2C). We  
172 observed that populations S1, S4, and S9 had the highest sedimentation rates at the end of  
173 the evolution experiment (Figure 2C). We observed a dramatic increase in sedimentation rate  
174 already after 14 transfers for population S1 (~91 generations) (Figure 2C). To assess and  
175 compare the variability in sedimentation rates among evolved lineages, we isolated and  
176 characterized a single clone from each evolved culture. Our results show that evolved clones  
177 all settled significantly faster than the common ancestor, but that there was stark variation in  
178 sedimentation rates at the end of the EE (Figure 2D). Moreover, the lineages can be roughly  
179 sorted into three classes based on settling speed (slow, intermediate and fast-settling) (Figure  
180 2D), with isolates from lineages S1, S4 and S9 settled the fastest upon sedimentation (Video

181 1), while clones from lineages S2, S3, S5 and S7 were intermediate, and lineages S6, S8 and  
182 S10 settled the slowest (Figure 2D). Taken together, our results show that we can rapidly and  
183 routinely evolve fast-settling mutants in *S. arctica* using experimental evolution, but that the  
184 outcome is not uniform across lineages.

185 We next sought to characterize the cellular mechanisms giving rise to variation in cellular  
186 sedimentation rates in evolved clones. Using quantitative microscopy, we show that clump  
187 radius and average number of cells observed per clump correlated highly with sedimentation  
188 rates (Figure 2E and Figure 2- supplement figure 1C, D and E). Indeed, across all experiments  
189 reported in this study, we found that using Stokes' law, a single globally fitted density  
190 parameter and our size measurements, could explain the majority of variance in sedimentation  
191 rate ( $R^2 = 0.69$ , RMSE (as a proportion of the range in observations) = 18%).

### 192 **Fast-sedimenting mutants form clonal clumps**

193 Earlier, we defined three distinct developmental stages of *S. arctica* life cycle: (i) cell growth  
194 with an increase in coenocyte volume, (ii) cellularization which coincides with actomyosin  
195 network formation and plasma membrane invaginations, and (iii) release of new-born cells  
196 (Figure 1B) (Dudin et al., 2019). A key developmental movement named “flip”, defined by an  
197 abrupt internal morphological change in the coenocyte, can be used as a reference point to  
198 characterize life cycle stages. Prior to this event (pre-flip), actomyosin-dependent plasma  
199 membrane invaginations occur, while afterwards (post-flip) the cell wall is formed around  
200 individual cells prior to their release from the coenocyte (Dudin et al., 2019). Using time-lapse  
201 microscopy at 12°C, we observed that clump formation in fast-settling mutants coincides with  
202 cell release (Figure 3A, Video 2).

203 Importantly, no new cell aggregation processes were detected after cell release, suggesting  
204 that all clumps formed either prior to or concomitantly with the release of new-born cells (Video  
205 2). To examine whether clumps formed due to defects at the level of either plasma membrane  
206 or cell wall, we stained plasma membranes using FM4-64 and cell walls using calcofluor-white.  
207 We found that the process of plasma membrane invaginations during cellularization appears  
208 to be unchanged prior to flip (Figure 3B- Video 3), and that all new-born cells, even in the  
209 clumps, have a distinctive cell wall surrounding them (Figure 3C, Figure 3- figure supplement  
210 1A). These results show that clumps are formed post-flip in fast-settling mutants.

211 As no cells appear to aggregate after release of new-born cells, our results suggest that  
212 clumps are maintained together in a clonal form. To further confirm this, we sonicated both  
213 the ancestor (AN) and S1 clumps and stained them separately with two distinct fluorescent  
214 dyes prior to mixing them in a 1:1 ratio (Figure 3- figure supplement 1B). After one complete

215 life-cycle, we observed that out of 198 clumps, the largest 183 contained only evolved S1  
216 derivatives, whereas ancestral cells only sporadically formed clumps under the conditions of the  
217 experiment (a total of 12 small clumps). Only 3 of the clumps (~1.5%) contained cells of both  
218 colours (Figure 3- figure supplement 1B), and each only contained a single AN cell trapped  
219 inside a smaller S1 clump. In a control experiment with two differentially stained S1 cultures,  
220 we observed an almost identically small number (i.e., ~1.7%) of mixed clumps (Figure 3- figure  
221 supplement 1B), hence, it appears that mixes of cells happen only sporadically at low  
222 frequencies by random association, irrespective of genotype. Altogether, our results suggest  
223 that the evolved clump phenotype is not a result of spontaneous cell aggregation, and instead  
224 arises from incomplete detachment between daughter and mother cells.

225 We next examined the kinetics of cellularization and the process by which cells propagate as  
226 part of clumps. We counted the number of cells detaching from clumps at cell release and  
227 observed a variable extent of detachment across all three fast-settling mutants. The clumpiest  
228 isolate, population S1, was the least prone to cell detachment (Figure 3A and D, Videos 2, 3).  
229 Intriguingly, despite exhibiting similar sedimentation rates, S4 and S9 clumps showed a higher  
230 detachment frequency than S1 (Figure 3A and D). Image analysis of time-lapse movies also  
231 showed that life-stage durations varied among fast-settling mutants at 12°C, with S1, S4, and  
232 S9 initiating cellularization and undergoing flip 5,5 hours, 7,5 and 10,5 hours, respectively,  
233 earlier than the ancestor (Figure 3- figure supplement 1C-D). Post-flip duration also varied  
234 significantly among mutants, with S1 and S9 requiring more time to release cells compared to  
235 S4 (Figure 3- figure supplement 1C-D). While many aspects of the replication cycle dynamics  
236 were variable for these mutants, the duration of cellularization was fairly invariant (~ 9 hours)  
237 (Figure 3- figure supplement 1C-D). Finally, measurements of coenocyte volume show that  
238 S4 and S9 coenocytes undergo flip at substantially smaller volumes (~1,8 and ~3,3x times  
239 smaller respectively) compared to AN or S1 (Figure 3E). These results show that, despite their  
240 shared capacity to clump and similar sedimentation rates, fast-settling mutants exhibit  
241 significant variability in life cycle dynamics, with S4 and S9 mutants initiating cellularization  
242 earlier, dispersing from clumps with a higher frequency, and undergoing flip and cell release  
243 at smaller coenocyte volumes compared to the S1 mutant.

#### 244 **Increased nuclear number-to-volume ratio leads to faster sedimentation**

245 Above we observed that S4 and S9 mutants can sediment as fast as S1 despite their smaller  
246 coenocyte volumes, suggesting an alternative regulation mechanism of sedimentation rate.  
247 Across all experiments reported in this study, we found that ~18% of error in observations of  
248 sedimentation rate could not be explained by cell size only, suggesting that cellular density  
249 might also contribute to this variation (Eppley et al., 1967; SMAYDA & J., 1970; Smayda,



250 1971). From Stoke's law, we calculated that *excess cellular density*, i.e., cellular density minus  
251 that of distilled water (~~with~~  $1000 \text{ kg/m}^3$ ), might vary between 40 and  $300 \text{ kg/m}^3$  for *S. arctica*  
252 wild-type and evolved clones across their life cycle – the upper limits between the densities of  
253 pure protein and pure cellulose. Values reached  $\sim 650$  for wild *S. nootakensis* (*Snoo*) soon  
254 after cellularization, approaching the density of pure nucleic acid (Figure 1D). During cell cycle  
255 stages prior to cellularization, when cells were most spherical (<36 hours), density varied from  
256 40-200 across *Sphaeroforma* isolates.

257 To better characterize the relationship between sedimentation rate, cell cycle and size we  
258 performed higher resolution measurements of sedimentation rates over the complete life cycle  
259 of the ancestor and all three fast-settling mutants at  $12^\circ\text{C}$  and  $17^\circ\text{C}$ . Consistent with their  
260 capacity to form clumps, we observed that the sedimentation rate of all fast-settling mutants  
261 increases during growth but, unlike the ancestor, does not recover after cell release to their  
262 original levels (Figure 4A and figure 4-figure supplement 1A). Interestingly, we noticed that  
263 individual S4 and S9 coenocytes sediment faster ( $\sim 2.5\text{x}$  and  $\sim 1.6\text{x}$  respectively) than S1 or  
264 AN even before clump-formation (24 to 36 hours timepoints) (Figure 4A and figure 4-figure  
265 supplement 1A). Such increase in sedimentation rate was not due to a rise in cell size or  
266 change in cell shape as both S4 and S9 exhibit smaller cell perimeters throughout the cell  
267 cycle (Figure 4B, C and figure 4-figure supplement 1B, C). Rather, cellular density estimations  
268 show that both S4 and S9, even prior to cell release and clump formation, tend to be on  
269 average 3x denser when compared to the ancestor (Figure 4D and figure 4-figure supplement  
270 1D). Altogether, these results show that both cell size and cell density contribute to  
271 sedimentation rate variation in *S. arctica*.

272 As cell size and nuclear division cycles are decoupled in *S. arctica* (Ondracka et al., 2018),  
273 we reasoned that increased cell density in S4 and S9 could be caused by an acceleration of  
274 nuclear divisions leading to a rise in the number of nuclei per volume. Using DAPI staining to  
275 label nuclear DNA, we observed that S4 and S9 undergo nuclear duplication faster ( $\sim 2$  hours)  
276 than both AN and S1 (Figure 4E, F and figure 4-figure supplement 1E to H). By carefully  
277 examining the volumes of coenocytes containing the same number of nuclei at the single-cell  
278 level, we show that for the same nuclear content, S4 and S9 tend to be 30-45% smaller in  
279 volume when compared to the ancestor (Figure 4G and figure 4-figure supplement 1I).  
280 Consequently, both S4 and S9 exhibited the highest number of nuclei per volume (nuclear  
281 number-to-volume ratio) (Figure 4H and figure 4-figure supplement 1J). Taken together, these  
282 results argue that cell density can contribute an appreciable amount to cellular sedimentation  
283 rates (up to  $\sim 50 \mu\text{m/s}$ ), and that mechanistically this could arise by faster nuclear doubling  
284 times relative to cell size.

## 285 **Evolved genetic variation correlating with fast sedimentation**

286 Up to now, our results suggest that *S. arctica* mutants evolved faster sedimentation using two  
287 strategies: (i) clump formation, and (ii) increasing the nuclear number-to-volume ratio. We  
288 found that sedimentation rate variation was highly heritable, surviving 780 generations of  
289 passaging for all 10 isolates without selection for sedimentation phenotype, suggesting that  
290 the phenotypes have a genetic basis. To test this, we sequenced the whole genomes of both  
291 the ancestral clone (AN) and one evolved clone per lineage (S1-S10) obtained at the  
292 conclusion of the evolution experiment (Week 8). Following variant filtering (Figure 4-Source  
293 data 1 and 2), we identified a total of 26 independently evolved variants with an average of  
294 2.6 mutations per clone (range 1 to 5 per clone) (Figure 4-Source data 3). Of the 26 variants,  
295 24 (~92.3%) were SNPs (11 coding, and 13 intergenic or intronic), and two were insertions  
296 (one coding, one intergenic) (Figure 4-Source data 3). Two of these variants are identical  
297 SNPs at the same position (*Sarc4\_g3900*) and have independently evolved in two different  
298 backgrounds (Figure 4-Source data 3). Strikingly, we found that the coding SNP variants were  
299 skewed toward non-synonymous changes (9:2), with a cumulative dN:dS-ratio of 1.32. This  
300 indicates the general presence of positive selection, and hence adaptative evolution driving  
301 this molecular pattern.

302

303 To better understand how the distinct variants could have influenced sedimentation rates and  
304 clump formation, we examined the predicted expression dynamics of mutated genes across  
305 the cell cycle based on our recently published time-resolved transcriptomics dataset of the *S.*  
306 *arctica* life cycle (Dudin et al., 2019). Of the mutated genes, 9 show no expression during the  
307 native life cycle, 12 show dynamical expression during cellularization, while the remaining 5  
308 genes are more or less stably expressed (Figure 4 I-K, Figure 4- figure supplement 1K, Figure  
309 4- source data 4). We also annotated all mutation-associated genes based on a recent  
310 comprehensive orthology search (Grau-Bové et al., 2017) (Figure 4- source data 5).

311

312 The fastest-settling and clumpiest mutant isolated from the population S1, bore a synonymous  
313 mutation of a homolog of increased sodium tolerance 1 superfamily (*Ist1*). This gene shows  
314 a dynamic expression during cellularization and codes for a conserved protein involved in  
315 multivesicular body (MVB) protein sorting (Figure 4 I, Figure 4- source data 5) (Dimaano et  
316 al., 2008; Frankel et al., 2017). In humans, *hIST1* also known as *KIAA0174*, is a regulator of  
317 the endosomal sorting complex required for transport (ESCRT) pathway, and has been shown  
318 to be essential for cytokinesis in mammalian cells (Agromayor et al., 2009). Similarly, *Ist1*  
319 orthologs in both budding and fission yeasts play a role in MVB sorting pathway and, when  
320 deleted, exhibit a multiseptated phenotype consistent with a role in cytokinesis and cell  
321 separation (Dudin et al., 2017; Xiao et al., 2009).

322

323 In the clone derived from population S4, we observed five distinct mutations, two  
324 nonsynonymous, one intergenic and two intronic SNPs. Among the two nonsynonymous  
325 SNPs, one causes a E90G change in a homolog of human Kanadaptin (SLC4A1AP), which  
326 may play a role in signal transduction (Hübner et al., 2002, 2003). Among the non-coding  
327 SNPs, one mutation is found in an intron of the 7-dehydrocholesterol reductase (DHCR7),  
328 expressed during cellularization and known to be key in the cholesterol biosynthesis pathway,  
329 (Fitzky et al., 1998; Prabhu et al., 2016), and the second intronic mutation codes for a STE20-  
330 like kinase (SLK) which plays numerous roles in cell-cycle signalling and actin cytoskeleton  
331 regulation (Figure 4 J) (Al-Zahrani et al., 2013; Cvrčková et al., 1995; Rohlf et al., 2007; Y.  
332 Wang et al., 2020).

333

334 Finally, among the five mutations discovered in the clone derived from population S9, two  
335 mutations are in transcription factors that are continually expressed during the cell cycle: an  
336 intronic SNP in a basic helix-loop-helix (bHLH) transcription factor, and the sole  
337 nonsynonymous SNP leading to A923V change in a gene predicted to encode a nucleotide  
338 binding C2H2 Zn finger domain (Fedotova et al., 2017). A third mutation was found in an intron  
339 of the highly and dynamically expressed homolog of the regulator of chromosome  
340 condensation 1 (RCC1; Figure 4 K) (Dasso, 1993; Hadjebi et al., 2008; Qiao et al., 2018).  
341 Importantly, this mutation may contribute to the accelerated nuclear duplication cycle  
342 observed in S9, by impacting cell-cycle progression. Altogether, the mutations identified in  
343 both S4 and S9 may affect both cellularization and cell separation.

344

345 Among the variants detected in evolved clones with intermediate-settling phenotype, we  
346 highlight an intergenic mutation 128bp downstream of Dynamin-1 known to be essential for  
347 cytokinesis across different taxa (Konopka et al., 2006; Masud Rana et al., 2013; Rikhy et al.,  
348 2015), and a nonsynonymous mutation in a protein similar to Fibrillin-2 (Sarc4\_g7365T) which  
349 is an extracellular matrix (ECM) glycoprotein essential for the formation of elastic fibres in  
350 animals (Figure 4- figure supplement 1K) (M. C. Wang et al., 2009; Yin et al., 2019; Zhang et  
351 al., 1994). Altogether, our results suggest a large mutational target affects cellular  
352 sedimentation and multicellularity.

### 353 **Sedimentation rate variation across *Sphaeroforma* species is driven by cell size and** 354 **density**

355 Lastly, we examined whether the variation in cell sedimentation observed across different  
356 *Sphaeroforma* species (Figure 1E) could also be explained by clumping or increased nuclear  
357 number-to-volume ratio. To do so, we investigated the life cycle dynamics, coenocyte volume

358 and nuclear duplication time among distinct *Sphaeroforma* sister species. To date, six different  
359 *Sphaeroforma* species have been isolated either in a free-living form or derived from different  
360 marine hosts: *S. arctica*, *S. sirkka*, *S. napiecek*, *S. tapetis*, *S. gastrica* and *S. nootakensis*  
361 (Figure 5A) (Ducluzeau et al., 2018; Dudin et al., 2019; Hassett et al., 2015; Jøstensen et al.,  
362 2002; W. L. Marshall et al., 2008; W. L. Marshall & Berbee, 2013). Using previously  
363 established growth methods for *S. arctica* combined with live and fixed imaging we first  
364 observed that all sister species but *S. tapetis* show a synchronized coenocytic life cycle (Figure  
365 5B, figure 5-figure supplement 1A, Video 4) (Similar observations were also made by A.  
366 Ondracka; personal communication). Similar to above mentioned results with fast-settling  
367 mutants, sedimentation rate variations (Figure 1E), could be explained by variations in both  
368 cell size and cellular density. Indeed, we first observed that both *S. gastrica* and *S.*  
369 *nootakensis* occasionally form clumps, exhibit a lower frequency of cell detachment and thus  
370 have an increased cellular density after cell release compared to the other *Sphaeroforma*  
371 species (Figures 1C, 5B and C, Video 4). Additionally, despite their increased sedimentation  
372 rate (Figure 1C), we found that all sister species exhibited ~20-45% smaller coenocyte size  
373 prior to cell-release when compared to *S. arctica* which reveals an increased cellular density  
374 (Figure 5D and figure 5-figure supplement 1B to D, Video 4). Similar to the fast-settling  
375 mutants S4 and S9 above, the increase in cellular density was associated with an acceleration  
376 of the nuclear division cycles and the subsequent rise in the nuclear number-to-volume ratio  
377 (Figure 5D-F and figure 5-figure supplement 1D- F). Notably, *S. sirkka* and *S. napiecek*, both  
378 previously isolated as free-living (Ducluzeau et al., 2018; W. L. Marshall & Berbee, 2013),  
379 exhibit an increase in nuclear number-to-volume ratio but no ability to form clumps. Altogether,  
380 our results show that, similarly to experimentally evolved strains, fast sedimentation variation  
381 could occur by both clump formation and/or increase in the nuclear number-to-volume ratio  
382 for *Sphaeroforma* species and thus might represent in itself a widespread and highly variable  
383 phenotype in the marine habitat.

## 384 Discussion

385

386 Our results demonstrate that, under suitable selection pressure, the unicellular holozoan  
387 *Sphaeroforma arctica* - a close relative of animals, can evolve stable multicellularity. In  
388 particular, we observed the independent rise of clump-formation, and faster settling  
389 phenotypes across populations within less than 400 generations. The precise detectable onset  
390 of the phenotypes varied across lineages, and occurred as early as ~91 generations in lineage  
391 S1. Our results add to previous observations of rapid emergence of multicellularity in yeast  
392 and green algae, which all can evolve multicellular clump-forming structures within short  
393 evolutionary timescales (Herron et al., 2019; Ratcliff et al., 2012, 2013). As ichthyosporeans

394 proliferate through an uncommon coenocytic life cycle (A. de Mendoza et al., 2015; Dudin et  
395 al., 2019; Suga & Ruiz-Trillo, 2013), our results show that this cellular process is accessible  
396 at microevolutionary timescales across taxa and organisms with highly diverged modes of  
397 proliferation.

398

399 In this study, we show that all fast-settling *S. arctica* cells increased their cell size by increasing  
400 cell-cell adhesion post-cellularization, leading to the formation of clumps. Such results are  
401 analogous to cell cluster formation in snowflake yeast and *Chlamydomonas reinhardtii* which  
402 arises through incomplete separation of mother and daughter cells (Koschwanez et al., 2013;  
403 Ratcliff et al., 2012, 2013). Altogether, these results suggest that regulation of sedimentation  
404 rate can constrain unicellular species to generate multicellular cell phenotypes by increasing  
405 their cell adhesion efficiency. However, we found that ~20% of variance could not be explained  
406 by cell (clump) size only. Indeed, two fast-settling mutants (S4, S9), exhibited an increase in  
407 sedimentation rate prior to clump formation, which was associated with an accelerated nuclear  
408 division cell cycle leading to an increase in the number of nuclei per volume. Previous results  
409 have shown that, in *S. arctica*, both nuclear duplication cycles and cell size are uncoupled  
410 (Ondracka et al., 2018). Our results support these findings and indicate that nuclear division  
411 cycles and cell size could be regulated separately, allowing adaptive change in either, and  
412 independently of one another.

413

414 By analysing the genomes of evolved isolates, we identified an abundance of non-  
415 synonymous mutations, indicating positive selection, with at least one and up to five  
416 independent mutations in each lineage. Many of the better-characterized genes that carry  
417 mutations in either coding or intergenic regions are dynamically expressed during  
418 cellularization. Several mutations were found in genes involved in cell signalling, plasma  
419 membrane remodelling and chromatin condensation regulators reflecting a large and  
420 accessible mutational target affecting sedimentation rate phenotypes. Given that similar  
421 phenotypes emerged independently multiple times with no genetic overlap, we conclude that  
422 the mutational target for these traits could be quite large for *S. arctica*, opening the possibility  
423 for variation and evolution in multicellularity-related phenotypes. We found that closely related  
424 species exhibit widespread variation in both clump formation and nuclei-to-volume ratio. Given  
425 the evolvability of the trait, it is difficult to argue whether clumpiness is an 'ancestral' trait, and  
426 it could represent a phenotype which is quickly gained and lost. It seems more likely that these  
427 species could naturally vary their degree of clumpiness and density over short  
428 microevolutionary timescales such as those we have measured in the lab.

429 Indeed, marine organisms have evolved various passive or active means of maintaining their  
430 position in the water column, for example using motility and/or ingenious approaches to  
431 regulate buoyancy (Chen et al., 2019; N. B. Marshall, 1954; Pfeifer, 2015; Strand et al., 2005;  
432 Sundby & Kristiansen, 2015; Villareal & Carpenter, 2003). *Sphaeroforma* species are  
433 remarkably spherical, immobile, lack flagella and yet exhibit a substantial increase in cell size  
434 and density over the life cycle, thus representing a challenge to maintaining buoyancy in  
435 marine habitat. This work establishes that *Sphaeroforma*'s cell size and density are subject to  
436 tight cellular control and are highly evolvable traits. Taken together, these observations  
437 suggest that sedimentation rate is a highly variable trait which itself likely shapes the gain and  
438 loss of multicellularity.

#### 439 **Author contributions**

440 O.D. designed the study, performed all the experiments and analysed the data.  
441 S.W. analysed and annotated all the genomes from this study. A.M.N. analysed data and  
442 models of sedimentation rate. O.D., S.W. and A.M.N. wrote the original draft. O.D. and I.R.T  
443 obtained funding. All authors reviewed and edited the manuscript.

444

#### 445 **Acknowledgments**

446 We thank Macarena Toll Riera, Pierre Gönczy, Gautam Dey, Andrej Ondracka for discussion  
447 and comments on the manuscript, Hiroshi Suga, Xavi Grau-Bové for advice on genome  
448 analysis, Jon Bråte for cultures of the different *Sphaeroforma* sister species, and Meritxell  
449 Antó for technical support.

450 We also acknowledge the CRG Genomics Unit for mRNA library preparation and Illumina  
451 sequencing. This work was funded by European Research Council Consolidator Grant (ERC-  
452 2012-Co -616960) to I.R.-T.; O.D. was supported by a Swiss National Science Foundation  
453 Early PostDoc Mobility fellowship (P2LAP3\_171815) a Marie Skłodowska-Curie individual  
454 fellowship (MSCA-IF 746044) and by an Ambizione fellowship from the Swiss National  
455 Science Foundation (PZ00P3\_185859).

456

#### 457 **Declaration of interests**

458 The authors declare no competing interests

459

#### 460 **References**

461 Agromayor, M., Carlton, J. G., Phelan, J. P., Matthews, D. R., Carlin, L. M., Ameer-Beg, S.,  
462 Bowers, K., & Martin-Serrano, J. (2009). Essential role of hIISTI in cytokinesis.  
463 *Molecular Biology of the Cell*. <https://doi.org/10.1091/mbc.E08-05-0474>  
464 Al-Zahrani, K. N., Baron, K. D., & Sabourin, L. A. (2013). Ste20-like kinase SLK, at the

- 465       crossroads: A matter of life and death. In *Cell Adhesion and Migration*.  
466       <https://doi.org/10.4161/cam.22495>
- 467   Alegado, R. A., Brown, L. W., Cao, S., Dermenjian, R. K., Zuzow, R., Fairclough, S. R.,  
468       Clardy, J., & King, N. (2012). A bacterial sulfonolipid triggers multicellular development  
469       in the closest living relatives of animals. *ELife*. <https://doi.org/10.7554/eLife.00013>
- 470   Allen, W. E. (1932). Problems of Flotation and Deposition of Marine Plankton Diatoms.  
471       *Transactions of the American Microscopical Society*, 51(1), 1.  
472       <https://doi.org/10.2307/3222044>
- 473   Andrews, S. (2010). FastQC - A quality control tool for high throughput sequence data.  
474       <http://www.bioinformatics.babraham.ac.uk/projects/fastqc/>. *Babraham Bioinformatics*.
- 475   Bao, W., Kojima, K. K., & Kohany, O. (2015). Repbase Update, a database of repetitive  
476       elements in eukaryotic genomes. *Mobile DNA*. [https://doi.org/10.1186/s13100-015-](https://doi.org/10.1186/s13100-015-0041-9)  
477       0041-9
- 478   Beardall, J., Allen, D., Bragg, J., Finkel, Z. V., Flynn, K. J., Quigg, A., Rees, T. A. V.,  
479       Richardson, A., & Raven, J. A. (2009). Allometry and stoichiometry of unicellular,  
480       colonial and multicellular phytoplankton. *New Phytologist*, 181(2), 295–309.  
481       <https://doi.org/10.1111/j.1469-8137.2008.02660.x>
- 482   Bonner, J. T. (1998). The origins of multicellularity. *Integrative Biology: Issues, News, and*  
483       *Reviews*, 1(1), 27–36. [https://doi.org/10.1002/\(SICI\)1520-6602\(1998\)1:1<27::AID-](https://doi.org/10.1002/(SICI)1520-6602(1998)1:1<27::AID-INBI4>3.0.CO;2-6)  
484       INBI4>3.0.CO;2-6
- 485   Brunet, T., & King, N. (2017). The Origin of Animal Multicellularity and Cell Differentiation. In  
486       *Developmental Cell*. <https://doi.org/10.1016/j.devcel.2017.09.016>
- 487   Brunet, T., Larson, B. T., Linden, T. A., Vermeij, M. J. A., McDonald, K., & King, N. (2019).  
488       Light-regulated collective contractility in a multicellular choanoflagellate. *Science (New*  
489       *York, N.Y.)*. <https://doi.org/10.1126/science.aay2346>
- 490   Chen, M., Tian, L. L., Ren, C. Y., Xu, C. Y., Wang, Y. Y., & Li, L. (2019). Extracellular  
491       polysaccharide synthesis in a bloom-forming strain of *Microcystis aeruginosa*:  
492       implications for colonization and buoyancy. *Scientific Reports*.  
493       <https://doi.org/10.1038/s41598-018-37398-6>
- 494   Cvrčková, F., De Virgilio, C., Manser, E., Pringle, J. R., & Nasmyth, K. (1995). Ste20-like  
495       protein kinases are required for normal localization of cell growth and for cytokinesis in  
496       budding yeast. *Genes and Development*. <https://doi.org/10.1101/gad.9.15.1817>
- 497   Dasso, M. (1993). RCC1 in the cell cycle: the regulator of chromosome condensation takes  
498       on new roles. *Trends in Biochemical Sciences*. [https://doi.org/10.1016/0968-](https://doi.org/10.1016/0968-0004(93)90161-F)  
499       0004(93)90161-F
- 500   de Mendoza, A., Suga, H., Permanyer, J., Irimia, M., & Ruiz-Trillo, I. (2015). Complex  
501       transcriptional regulation and independent evolution of fungal-like traits in a relative of

- 502 animals. *ELife*, 4. <https://doi.org/10.7554/eLife.08904>
- 503 Deatherage, D. E., & Barrick, J. E. (2014). Identification of mutations in laboratory-evolved  
504 microbes from next-generation sequencing data using breseq. *Methods in Molecular*  
505 *Biology*. [https://doi.org/10.1007/978-1-4939-0554-6\\_12](https://doi.org/10.1007/978-1-4939-0554-6_12)
- 506 Dimaano, C., Jones, C. B., Hanono, A., Curtiss, M., & Babst, M. (2008). Ist1 regulates Vps4  
507 localization and assembly. *Molecular Biology of the Cell*.  
508 <https://doi.org/10.1091/mbc.E07-08-0747>
- 509 Ducluzeau, A.-L., Tyson, J. R., Collins, R. E., Snutch, T. P., & Hassett, B. T. (2018).  
510 Genome Sequencing of Sub-Arctic Mesomycetozoean Sphaeroforma sirkka Strain B5,  
511 Performed with the Oxford Nanopore minION and Illumina HiSeq Systems.  
512 *Microbiology Resource Announcements*. <https://doi.org/10.1128/mra.00848-18>
- 513 Dudin, O., Merlini, L., Bendezú, F. O., Groux, R., Vincenzetti, V., & Martin, S. G. (2017). A  
514 systematic screen for morphological abnormalities during fission yeast sexual  
515 reproduction identifies a mechanism of actin aster formation for cell fusion. *PLoS*  
516 *Genetics*, 13(4). <https://doi.org/10.1371/journal.pgen.1006721>
- 517 Dudin, O., Ondracka, A., Grau-Bové, X., Haraldsen, A. A. B., Toyoda, A., Suga, H., Bråte, J.,  
518 & Ruiz-Trillo, I. (2019). A unicellular relative of animals generates a layer of polarized  
519 cells by actomyosin-dependent cellularization. *ELife*, 8.  
520 <https://doi.org/10.7554/eLife.49801>
- 521 Elena, S. F., & Lenski, R. E. (2003). Evolution experiments with microorganisms: the  
522 dynamics and genetic bases of adaptation. *Nature Reviews Genetics*, 4(6), 457–469.  
523 <https://doi.org/10.1038/nrg1088>
- 524 Eppley, R. W., Holmes, R. W., & Strickland, J. D. H. (1967). Sinking rates of marine  
525 phytoplankton measured with a fluorometer. *Journal of Experimental Marine Biology*  
526 *and Ecology*, 1(2), 191–208. [https://doi.org/10.1016/0022-0981\(67\)90014-7](https://doi.org/10.1016/0022-0981(67)90014-7)
- 527 Fairclough, S. R., Dayel, M. J., & King, N. (2010). Multicellular development in a  
528 choanoflagellate. In *Current Biology*. <https://doi.org/10.1016/j.cub.2010.09.014>
- 529 Fedotova, A. A., Bonchuk, A. N., Mogila, V. A., & Georgiev, P. G. (2017). C2H2 zinc finger  
530 proteins: The largest but poorly explored family of higher eukaryotic transcription  
531 factors. In *Acta Naturae*. <https://doi.org/10.32607/20758251-2017-9-2-47-58>
- 532 Finkel, Z. V., Beardall, J., Flynn, K. J., Quigg, A., Rees, T. A. V., & Raven, J. A. (2010).  
533 Phytoplankton in a changing world: Cell size and elemental stoichiometry. In *Journal of*  
534 *Plankton Research* (Vol. 32, Issue 1, pp. 119–137). Oxford Academic.  
535 <https://doi.org/10.1093/plankt/fbp098>
- 536 Fisher, R. M., Cornwallis, C. K., & West, S. A. (2013). Group formation, relatedness, and the  
537 evolution of multicellularity. *Current Biology*, 23(12), 1120–1125.  
538 <https://doi.org/10.1016/j.cub.2013.05.004>



- 539 Fitzky, B. U., Witsch-Baumgartner, M., Erdel, M., Lee, J. N., Paik, Y. K., Glossmann, H.,  
540 Utermann, G., & Moebius, F. F. (1998). Mutations in the  $\Delta 7$ -sterol reductase gene in  
541 patients with the Smith-Lemli-Opitz syndrome. *Proceedings of the National Academy of*  
542 *Sciences of the United States of America*. <https://doi.org/10.1073/pnas.95.14.8181>
- 543 FOURNIER, R. O. (1968). OBSERVATIONS OF PARTICULATE ORGANIC CARBON IN  
544 THE MEDITERRANEAN SEA AND THEIR RELEVANCE TO THE DEEP-LIVING  
545 COCCOLITHOPHORID CYCLOCOCOLITHUS FRAGILIS. In *Limnology and*  
546 *Oceanography* (Vol. 13, Issue 4, pp. 693–697). John Wiley & Sons, Ltd.  
547 <https://doi.org/10.4319/lo.1968.13.4.0693>
- 548 Frankel, E. B., Shankar, R., Moresco, J. J., Yates, J. R., Volkmann, N., & Audhya, A. (2017).  
549 Ist1 regulates ESCRT-III assembly and function during multivesicular endosome  
550 biogenesis in *Caenorhabditis elegans* embryos. *Nature Communications*.  
551 <https://doi.org/10.1038/s41467-017-01636-8>
- 552 Friebele, E. S., Correll, D. L., & Faust, M. A. (1978). Relationship between phytoplankton cell  
553 size and the rate of orthophosphate uptake: in situ observations of an estuarine  
554 population. *Marine Biology*, 45(1), 39–52. <https://doi.org/10.1007/BF00388976>
- 555 Gemmell, B. J., Oh, G., Buskey, E. J., & Villareal, T. A. (2016). Dynamic sinking behaviour in  
556 marine phytoplankton: Rapid changes in buoyancy may aid in nutrient uptake.  
557 *Proceedings of the Royal Society B: Biological Sciences*, 283(1840).  
558 <https://doi.org/10.1098/rspb.2016.1126>
- 559 Glockling, S. L., Marshall, W. L., & Gleason, F. H. (2013). Phylogenetic interpretations and  
560 ecological potentials of the Mesomycetozoa (Ichthyosporea). In *Fungal Ecology* (Vol.  
561 6, Issue 4, pp. 237–247). Elsevier Ltd. <https://doi.org/10.1016/j.funeco.2013.03.005>
- 562 Grau-Bové, X., Torruella, G., Donachie, S., Suga, H., Leonard, G., Richards, T. A., & Ruiz-  
563 Trillo, I. (2017). Dynamics of genomic innovation in the unicellular ancestry of animals.  
564 *ELife*. <https://doi.org/10.7554/eLife.26036>
- 565 Grosberg, R. K., & Strathmann, R. R. (2007). The evolution of multicellularity: A minor major  
566 transition? In *Annual Review of Ecology, Evolution, and Systematics*.  
567 <https://doi.org/10.1146/annurev.ecolsys.36.102403.114735>
- 568 Hadjebi, O., Casas-Terradellas, E., Garcia-Gonzalo, F. R., & Rosa, J. L. (2008). The RCC1  
569 superfamily: From genes, to function, to disease. In *Biochimica et Biophysica Acta -*  
570 *Molecular Cell Research*. <https://doi.org/10.1016/j.bbamcr.2008.03.015>
- 571 Hassett, B. T., López, J. A., & Gradinger, R. (2015). Two New Species of Marine  
572 Saprotrophic Sphaeroformids in the Mesomycetozoa Isolated From the Sub-Arctic  
573 Bering Sea. *Protist*. <https://doi.org/10.1016/j.protis.2015.04.004>
- 574 Herron, M. D., Borin, J. M., Boswell, J. C., Walker, J., Chen, I. C. K., Knox, C. A., Boyd, M.,  
575 Rosenzweig, F., & Ratcliff, W. C. (2019). De novo origins of multicellularity in response

- 576 to predation. *Scientific Reports*. <https://doi.org/10.1038/s41598-019-39558-8>
- 577 Hübner, S., Bahr, C., Gößmann, H., Efthymiadis, A., & Drenckhahn, D. (2003). Mitochondrial  
578 and nuclear localization of kanadaptin. *European Journal of Cell Biology*.  
579 <https://doi.org/10.1078/0171-9335-00308>
- 580 Hübner, S., Jans, D. A., Xiao, C. Y., John, A. P., & Drenckhahn, D. (2002). Signal- and  
581 importin-dependent nuclear targeting of the kidney anion exchanger 1-binding protein  
582 kanadaptin. *Biochemical Journal*. <https://doi.org/10.1042/0264-6021:3610287>
- 583 Jøstensen, J. P., Sperstad, S., Johansen, S., & Landfald, B. (2002). Molecular-phylogenetic,  
584 structural and biochemical features of a cold-adapted, marine ichthyosporean near the  
585 animal-fungal divergence, described from in vitro cultures. *European Journal of*  
586 *Protistology*. <https://doi.org/10.1078/0932-4739-00855>
- 587 Kawecki, T. J., Lenski, R. E., Ebert, D., Hollis, B., Olivieri, I., & Whitlock, M. C. (2012).  
588 Experimental evolution. In *Trends in Ecology and Evolution*.  
589 <https://doi.org/10.1016/j.tree.2012.06.001>
- 590 Knoll, A. H. (2011). The Multiple Origins of Complex Multicellularity. *Annual Review of Earth*  
591 *and Planetary Sciences*, 39(1), 217–239.  
592 <https://doi.org/10.1146/annurev.earth.031208.100209>
- 593 Konopka, C. A., Schleede, J. B., Skop, A. R., & Bednarek, S. Y. (2006). Dynamin and  
594 cytokinesis. In *Traffic*. <https://doi.org/10.1111/j.1600-0854.2006.00385.x>
- 595 Koschwanez, J. H., Foster, K. R., & Murray, A. W. (2013). Improved use of a public good  
596 selects for the evolution of undifferentiated multicellularity. *ELife*, 2013(2).  
597 <https://doi.org/10.7554/eLife.00367>
- 598 Leigh, E. G., Smith, J. M., & Szathmary, E. (1995). The Major Transitions of Evolution.  
599 *Evolution*. <https://doi.org/10.2307/2410462>
- 600 Levin, T. C., Greaney, A. J., Wetzell, L., & King, N. (2014). The Rosetteless gene controls  
601 development in the choanoflagellate *S. rosetta*. *ELife*.  
602 <https://doi.org/10.7554/eLife.04070>
- 603 Marshall, N. B. (1954). *Aspects of deep sea biology* (380 pp). Hutchinson.
- 604 Marshall, W. L., & Berbee, M. L. (2013). Comparative morphology and genealogical  
605 delimitation of cryptic species of sympatric isolates of sphaeroforma (Ichthyosporea,  
606 Opisthokonta). *Protist*. <https://doi.org/10.1016/j.protis.2012.12.002>
- 607 Marshall, W. L., Celio, G., McLaughlin, D. J., & Berbee, M. L. (2008). Multiple Isolations of a  
608 Culturable, Motile Ichthyosporean (Mesomycetozoa, Opisthokonta), *Creolimax*  
609 *fragrantissima* n. gen., n. sp., from Marine Invertebrate Digestive Tracts. *Protist*.  
610 <https://doi.org/10.1016/j.protis.2008.03.003>
- 611 Masud Rana, A. Y. K. M., Tsujioka, M., Miyagishima, S., Ueda, M., & Yumura, S. (2013).  
612 Dynamin contributes to cytokinesis by stabilizing actin filaments in the contractile ring.

- 613 *Genes to Cells*. <https://doi.org/10.1111/gtc.12060>
- 614 Mendoza, L., Taylor, J. W., & Ajello, L. (2002). The class Mesomycetozoa: A  
615 heterogeneous group of microorganisms at the animal-fungal boundary. In *Annual*  
616 *Review of Microbiology* (Vol. 56, pp. 315–344). Annu Rev Microbiol.  
617 <https://doi.org/10.1146/annurev.micro.56.012302.160950>
- 618 Millero, F. J., & Huang, F. (2009). The density of seawater as a function of salinity (5 to 70 g  
619 kg<sup>-1</sup>) and temperature (273.15 to 363.15 K). *Ocean Science*, 5(2), 91–100.  
620 <https://doi.org/10.5194/os-5-91-2009>
- 621 Niklas, K. J., & Newman, S. A. (2013). The origins of multicellular organisms. *Evolution and*  
622 *Development*, 15(1), 41–52. <https://doi.org/10.1111/ede.12013>
- 623 Ondracka, A., Dudin, O., & Ruiz-Trillo, I. (2018). Decoupling of Nuclear Division Cycles and  
624 Cell Size during the Coenocytic Growth of the Ichthyosporean *Sphaeroforma arctica*.  
625 *Current Biology*, 28(12). <https://doi.org/10.1016/j.cub.2018.04.074>
- 626 Oud, B., Guadalupe-Medina, V., Nijkamp, J. F., De Ridder, D., Pronk, J. T., Van Maris, A. J.  
627 A., & Daran, J. M. (2013). Genome duplication and mutations in ACE2 cause  
628 multicellular, fast-sedimenting phenotypes in evolved *Saccharomyces cerevisiae*.  
629 *Proceedings of the National Academy of Sciences of the United States of America*,  
630 110(45), E4223–E4231. <https://doi.org/10.1073/pnas.1305949110>
- 631 Parfrey, L. W., & Lahr, D. J. G. (2013). Multicellularity arose several times in the evolution of  
632 eukaryotes. *BioEssays*. <https://doi.org/10.1002/bies.201200143>
- 633 Parra-Acero, H., Harcet, M., Sánchez-Pons, N., Casacuberta, E., Brown, N. H., Dudin, O., &  
634 Ruiz-Trillo, I. (2020). Integrin-Mediated Adhesion in the Unicellular Holozoan  
635 *Capsaspora owczarzaki*. *Current Biology*. <https://doi.org/10.1016/j.cub.2020.08.015>
- 636 Pérez-Posada, A., Dudin, O., Ocaña-Pallarès, E., Ruiz-Trillo, I., & Ondracka, A. (2020). Cell  
637 cycle transcriptomics of *Capsaspora* provides insights into the evolution of cyclin-CDK  
638 machinery. *PLoS Genetics*, 16(3). <https://doi.org/10.1371/journal.pgen.1008584>
- 639 Pfeifer, F. (2015). Haloarchaea and the formation of gas vesicles. In *Life*.  
640 <https://doi.org/10.3390/life5010385>
- 641 Prabhu, A. V., Luu, W., Sharpe, L. J., & Brown, A. J. (2016). Cholesterol-mediated  
642 degradation of 7-dehydrocholesterol reductase switches the balance from cholesterol to  
643 Vitamin D synthesis. *Journal of Biological Chemistry*.  
644 <https://doi.org/10.1074/jbc.M115.699546>
- 645 Qiao, L., Zheng, J., Tian, Y., Zhang, Q., Wang, X., Chen, J. J., & Zhang, W. (2018).  
646 Regulator of chromatin condensation 1 abrogates the G1 cell cycle checkpoint via Cdk1  
647 in human papillomavirus E7-expressing epithelium and cervical cancer cells article. *Cell*  
648 *Death and Disease*. <https://doi.org/10.1038/s41419-018-0584-z>
- 649 Queller, D. C., Ponte, E., Bozzaro, S., & Strassmann, J. E. (2003). Single-gene greenbeard

- 650 effects in the social amoeba *Dictyostelium discoideum*. *Science*.  
651 <https://doi.org/10.1126/science.1077742>
- 652 Ratcliff, W. C., Denison, R. F., Borrello, M., & Travisano, M. (2012). Experimental evolution  
653 of multicellularity. *Proceedings of the National Academy of Sciences of the United*  
654 *States of America*. <https://doi.org/10.1073/pnas.1115323109>
- 655 Ratcliff, W. C., Fankhauser, J. D., Rogers, D. W., Greig, D., & Travisano, M. (2015). Origins  
656 of multicellular evolvability in snowflake yeast. *Nature Communications*.  
657 <https://doi.org/10.1038/ncomms7102>
- 658 Ratcliff, W. C., Herron, M. D., Howell, K., Pentz, J. T., Rosenzweig, F., & Travisano, M.  
659 (2013). Experimental evolution of an alternating uni- and multicellular life cycle in  
660 *Chlamydomonas reinhardtii*. *Nature Communications*.  
661 <https://doi.org/10.1038/ncomms3742>
- 662 Rikhy, R., Mavrakakis, M., & Lippincott-Schwartz, J. (2015). Dynamin regulates metaphase  
663 furrow formation and plasma membrane compartmentalization in the syncytial  
664 *Drosophila* embryo. *Biology Open*. <https://doi.org/10.1242/bio.20149936>
- 665 Rohlf, M., Arasada, R., Batsios, P., Janzen, J., & Schleicher, M. (2007). The Ste20-like  
666 kinase SvkA of *Dictyostelium discoideum* is essential for late stages of cytokinesis.  
667 *Journal of Cell Science*. <https://doi.org/10.1242/jcs.012179>
- 668 Rokas, A. (2008). The molecular origins of multicellular transitions. In *Current Opinion in*  
669 *Genetics and Development* (Vol. 18, Issue 6, pp. 472–478). Elsevier Current Trends.  
670 <https://doi.org/10.1016/j.gde.2008.09.004>
- 671 Ruiz-Trillo, I., Burger, G., Holland, P. W. H., King, N., Lang, B. F., Roger, A. J., & Gray, M.  
672 W. (2007). The origins of multicellularity: a multi-taxon genome initiative. *Trends in*  
673 *Genetics*, 23(3), 113–118. <https://doi.org/10.1016/j.tig.2007.01.005>
- 674 Ruiz-Trillo, I., & de Mendoza, A. (2020). Towards understanding the origin of animal  
675 development. *Development (Cambridge, England)*. <https://doi.org/10.1242/dev.192575>
- 676 Sebé-Pedrós, A., Degnan, B. M., & Ruiz-Trillo, I. (2017). The origin of Metazoa: A unicellular  
677 perspective. In *Nature Reviews Genetics*. <https://doi.org/10.1038/nrg.2017.21>
- 678 Sebé-Pedrós, A., Irimia, M., del Campo, J., Parra-Acero, H., Russ, C., Nusbaum, C.,  
679 Blencowe, B. J., & Ruiz-Trillo, I. (2013). Regulated aggregative multicellularity in a  
680 close unicellular relative of metazoa. *ELife*, 2(2:e01287).  
681 <https://doi.org/10.7554/eLife.01287>
- 682 SMAYDA, & J., T. (1970). The suspension and sinking of phytoplankton in the sea.  
683 *Oceanogr. Mar. Biol. Ann. Rev.*, 8, 353–414. <https://ci.nii.ac.jp/naid/10009425107>
- 684 Smayda, T. J. (1971). Normal and accelerated sinking of phytoplankton in the sea. *Marine*  
685 *Geology*, 11(2), 105–122. [https://doi.org/10.1016/0025-3227\(71\)90070-3](https://doi.org/10.1016/0025-3227(71)90070-3)
- 686 Smit, A., Hubley, R., & Grenn, P. (2015). *RepeatMasker Open-4.0*. RepeatMasker Open.

- 687 Strand, E., Jørgensen, C., & Huse, G. (2005). Modelling buoyancy regulation in fishes with  
688 swimbladders: Bioenergetics and behaviour. *Ecological Modelling*.  
689 <https://doi.org/10.1016/j.ecolmodel.2004.12.013>
- 690 Strassmann, J. E., Gilbert, O. M., & Queller, D. C. (2011). Kin discrimination and cooperation  
691 in microbes. In *Annual Review of Microbiology*.  
692 <https://doi.org/10.1146/annurev.micro.112408.134109>
- 693 Suga, H., & Ruiz-Trillo, I. (2013). Development of ichthyosporeans sheds light on the origin  
694 of metazoan multicellularity. *Developmental Biology*.  
695 <https://doi.org/10.1016/j.ydbio.2013.01.009>
- 696 Sundby, S., & Kristiansen, T. (2015). The principles of buoyancy in Marine Fish Eggs and  
697 their vertical distributions across the World Oceans. *PLoS ONE*.  
698 <https://doi.org/10.1371/journal.pone.0138821>
- 699 Tarnita, C. E., Taubes, C. H., & Nowak, M. A. (2013). Evolutionary construction by staying  
700 together and coming together. *Journal of Theoretical Biology*.  
701 <https://doi.org/10.1016/j.jtbi.2012.11.022>
- 702 Villareal, T. A., & Carpenter, E. J. (2003). Buoyancy regulation and the potential for vertical  
703 migration in the oceanic cyanobacterium *Trichodesmium*. *Microbial Ecology*.  
704 <https://doi.org/10.1007/s00248-002-1012-5>
- 705 Waite, A., Fisher, A., Thompson, P., & Harrison, P. (1997). Sinking rate versus cell volume  
706 relationships illuminate sinking rate control mechanisms in marine diatoms. *Marine  
707 Ecology Progress Series*, 157, 97–108. <https://doi.org/10.3354/meps157097>
- 708 Wang, M. C., Lu, Y., & Baldock, C. (2009). Fibrillin Microfibrils: A Key Role for the Interbead  
709 Region in Elasticity. *Journal of Molecular Biology*.  
710 <https://doi.org/10.1016/j.jmb.2009.02.062>
- 711 Wang, Y., Wang, R., & Tang, D. D. (2020). Ste20-like kinase-mediated control of actin  
712 polymerization is a new mechanism for thin filament-associated regulation of airway  
713 smooth muscle contraction. *American Journal of Respiratory Cell and Molecular  
714 Biology*. <https://doi.org/10.1165/RCMB.2019-0310OC>
- 715 Wickham, H. (2016). ggplot2: Elegant Graphics for Data Analysis. In *Journal of the Royal  
716 Statistical Society: Series A (Statistics in Society)*.
- 717 Wielgoss, S., Wolfensberger, R., Sun, L., Fiegna, F., & Velicer, G. J. (2019). Social genes  
718 are selection hotspots in kin groups of a soil microbe. *Science*.  
719 <https://doi.org/10.1126/science.aar4416>
- 720 Xiao, J., Chen, X. W., Davies, B. A., Saltiel, A. R., Katzmann, D. J., & Xu, Z. (2009).  
721 Structural basis of Ist1 function and Ist1-Did2 interaction in the multivesicular body  
722 pathway and cytokinesis. *Molecular Biology of the Cell*.  
723 <https://doi.org/10.1091/mbc.E09-05-0403>

724 Yin, W., Kim, H. T., Wang, S. P., Gunawan, F., Li, R., Buettner, C., Grohmann, B., Sengle,  
725 G., Sinner, D., Offermanns, S., & Stainier, D. Y. R. (2019). Fibrillin-2 is a key mediator  
726 of smooth muscle extracellular matrix homeostasis during mouse tracheal  
727 tubulogenesis. *European Respiratory Journal*. [https://doi.org/10.1183/13993003.00840-](https://doi.org/10.1183/13993003.00840-2018)  
728 2018

729 Zhang, H., Apfelroth, S. D., Hu, W., Davis, E. C., Sanguineti, C., Bonadio, J., Mecham, R.  
730 P., & Ramirez, F. (1994). Structure and expression of fibrillin-2, a novel microfibrillar  
731 component preferentially located in elastic matrices. *Journal of Cell Biology*.  
732 <https://doi.org/10.1083/jcb.124.5.855>

733

734

## 735 **Methods**

736

### 737 **Culture conditions**

738 All *Sphaeroforma sp.* cultures were grown and synchronized as described previously for  
739 *Sphaeroforma arctica* (Dudin et al., 2019; Ondracka et al., 2018) . Briefly, saturated cultures  
740 in Marine Broth (MB) (Difco BD, NJ, USA; 37.4g/L) were diluted into fresh medium at low  
741 density (1:250 dilution of the saturated culture) and grown in rectangular canted neck cell  
742 culture flask with vented cap (Falcon®; ref: 353108) at either 17°C or 12°C, resulting in a  
743 synchronously growing culture. Saturated culture of *Sphaeroforma sp.* are obtained after 3  
744 weeks of growth in MB.

### 745 **Experimental evolution**

746 Ten replicate population (S1 to S10) of genetically identical *Sphaeroforma arctica* (AN) were  
747 first diluted 250-fold in 5 ml of MB and grown in rectangular canted neck cell culture flask with  
748 vented cap (Falcon®; ref: 353108) at 17°C. Cells were grown at 17°C rather than the  
749 previously used 12°C in order to increase growth rates and accelerate evolutionary outcome.  
750 Every 24 hours, the entire population was transferred into a 15ml falcon tube and allowed to  
751 sediment for 2 min on the bench. A 5 ml pipette was then positioned vertically and used to  
752 collect 500µl of cell culture from the bottom of the falcon tube. The cells, still vertically  
753 positioned in the pipette, were then allowed to sediment once more for 15 second before the  
754 transfer of a single drop, equivalent to 20µl, into 5ml of fresh MB (~ 250x dilution). Every 7  
755 transfers, a frozen fossil was conserved by adding 10% of DMSO to 1ml of culture and  
756 preserved at -80°C. Single clones of each replicate population (S1 to S10) were obtained at  
757 the end of week 8 by serial dilutions. Since *S. arctica* grows as a coenocyte, a temporal  
758 generation is not defined by a complete coenocytic cycle, but is equivalent to the doubling of  
759 the number of nuclei. We estimated the nuclear doubling time by measuring the number of  
760 cells and the number of nuclei per cell for each transfer separately (Figure 2- Source data 1).  
761 Briefly, the entire EE experiment comprised ~364 generations, in which all populations  
762 underwent a total of 28 complete coenocytic cycles. Each coenocytic cycle included two 24  
763 hours sub-passages, and comprised a total of ~13 doublings (Figure 2—figure supplement  
764 1A, Figure 2- Source data 1). Importantly, the effective population size was kept in a very  
765 narrow range across sub-passages (at ~10<sup>5</sup>) and thus over the entire experiment (Figure 2—  
766 figure supplement 1A, Figure 2- Source data 1). Therefore, in evolutionary terms, the  
767 population size was consistently high enough to favor of natural selection over random

768 evolution throughout the course of the experiment. This assumption was reconfirmed  
769 genetically by deriving a dN:dS-ratio >1 from sequencing data (see main text).

770

### 771 **Sedimentation rate measurements**

772 Sedimentation rate was measured for *Sphaeroforma sp.* every 12 hours for a total of 72 hours  
773 unless indicated otherwise. To ensure reproducibility and homogeneous results, saturated  
774 *Sphaeroforma sp.* cultures were sonicated prior to the dilution in fresh MB media (250-fold  
775 dilution) using a Branson 450 Digital Sonifier (3 pulses of 15 sec, 10% amplitude). For each  
776 measurement, either obtained from different stages of the cell-cycle or from different  
777 *Sphaeroforma* species, 1ml of cell culture was added into a disposable plastic  
778 spectrophotometer cuvette (semi-micro, 1.5ml) and homogenized by vortex. Optical density  
779 (OD<sub>600</sub>) was measured using an Eppendorf® Biophotometer (Model #1631) at T=0,  
780 corresponding to the first time point after placing the cuvette in the spectrophotometer. The  
781 OD<sub>600</sub> was then continuously measured every 30 seconds for 3 minutes while cells were slowly  
782 sedimenting in the cuvette. To ensure that OD<sub>600</sub> measurements stayed within the detection  
783 limits of the spectrophotometer, early life-stages (T0-T48) were not diluted in the cuvette,  
784 whereas later life-stages (T60-T72) were diluted 1/100 in fresh MB media.

785 For assessing clump dissociation in Figure 2 - figure supplement 1B, AN or S1 cultures were  
786 incubated for 2 hours at 37°C in MB, artificial sea water (ASW) (Instant Ocean, 36 g/L) with  
787 different salt concentrations ( 18 g/L for 0.5X and 72g/L for 2X) to assess any effect of  
788 electrostatic forces, Phosphophate buffered saline (PBS) 1X (Sigma-Aldrich) with either  
789 Proteinase K at 200 µg/mL final concentration (New England Biolabs, Ipswich, MA, USA) to  
790 assess for any protein-dependent effect or sonication using a Branson 450 Digital Sonifier (3  
791 pulses of 15 sec, 10% amplitude). Only sonication resulted in dissociation of the clumps and  
792 a reduction in sedimentation rates.

793

### 794 **Maximum likelihood estimation of sedimentation velocity and cellular density based on** 795 **OD600 sedimentation rate assay**

796 To briefly summarize, we related our OD600 A.U. sedimentation rate measurements and  
797 radius measurements (Figure 1 – Source Data 1) to previously published datasets (SMAYDA  
798 & J., 1970) and (Millero & Huang, 2009) (Figure 1 – Source Data 2 and 3) to gain an estimate  
799 of our sedimentation rate measurements in metric units, which allowed maximum likelihood  
800 estimation of cellular densities based on these estimates (Figure 1 – Source Data 1).

801 We started by estimating the average radius of cells from perimeter measurements as



802 
$$R = \text{Perimeter} / (2 \cdot \pi i)$$

803 We estimated sedimentation velocity in our measurements by assuming OD600 (OD) changes  
804 at a constant proportional rate of change with respect to time  $t=0$  and  $t=1$  by:

805 
$$dODdt = - \frac{\log(OD_1/OD_0)}{t_1 - t_0}$$

806 This yielded a rate of change in arbitrary distance units per second which we next sought to  
807 relate to metric distance units. For this we turned to the datasets from (Eppley et al., 1967),  
808 compiled along with data from other studies by (SMAYDA & J., 1970) in his Appendix Table 1  
809 (our Figure 1 – Source Data 2). In this table, 39 observations included joint values of salt  
810 percentages (or seawater density) for measurement, temperature, cell diameters, and  
811 sedimentation rate measurements for various phytoplankton isolates.

812 For each of these observations, we calculated seawater density in experimental assays as SC  
813 + salinity where salinity constant SC = 35.16504/35 and the salinity is the salt content in  $g \cdot l^{-1}$   
814 (Millero & Huang, 2009). We estimated the specific gravity or density of media used in each  
815 sedimentation rate measurement based upon the dataset published by (Millero & Huang,  
816 2009) (Figure 1 – Source Data 3), using a second-order polynomial function of their density  
817 measurements as a function of salinity and temperature using R's  $lm()$  function. The error of  
818 this estimate is extremely low ( $<4e-3 \text{ kg} \cdot m^{-3}$ ) and was not propagated downstream.

819 We next calculated the density  $p_p$  of cells across observations based on sedimentation velocity  
820  $V$  in  $m \cdot s$ , cell radius  $R$  in  $m$  and media density  $p_f$  by rearrangement of the terminal velocity  
821 equation:

822 
$$Pp = Pf + \frac{9 \cdot \mu \cdot V}{2 \cdot g \cdot R^2}$$

823 Where dynamic viscosity  $\mu = 0.00109 \text{ Pa} \cdot s$  and gravitational acceleration  $g = 9.780 \text{ m} \cdot s^{-2}$ . This  
824 yielded a median phytoplankton excess density ( $p_p - 1000$ ) of  $139 \text{ kg} \cdot m^{-3}$  with a range of 30-  
825  $1300 \text{ kg} \cdot m^{-3}$ . Some density estimates exceeding protein ( $220 \text{ kg} \cdot m^{-3}$ ) and cellulose ( $500 \text{ kg} \cdot m^{-3}$ )  
826  $^3$ ) have previously been suggested to arise by calcide in diatoms (FOURNIER, 1968). We  
827 concluded that this method of estimating cell density yielded similar values to those published  
828 by e.g. (FOURNIER, 1968) and (Eppley et al., 1967). For downstream analyses, we excluded  
829 obvious outliers, including measurements of samples with densities exceeding that of  
830 cellulose, and measurements of *D. rex*, a large diatom which in the Smayda dataset exhibited  
831 extraordinarily low sedimentation rates given their size.

832 To estimate the sedimentation velocities of our dataset, we assumed that our data (Figure 1  
833 – Source Data 1) would fall within the typical measurement in the Smayda dataset (Figure 1  
834 – Source Data 2). For the outlier-excluded subset of the Smayda dataset, we calculated an  
835 expected sedimentation velocity for what we would measure in our experimental setup based  
836 on the specific gravity of the seawater formulation we used in our measurements (37.4 g/l or  
837 a solvent density of  $1028.9 \text{ kg}\cdot\text{m}^{-3}$ ). We then used least-squares minimization to estimate two  
838 parameters: a multiplicative scalar  $S$  of the AU velocity measurements,  $dODdt$ , which could  
839 best match our dataset with these expected velocities, and an average density parameter  
840  $\rho_{p\_hat}$  which could predict these values and the Smayda dataset's values based on Stokes'  
841 law. For this we minimized the loss function:

$$842 \quad \sum_i^N \left( V_0 \cdot S \cdot H - \frac{2 \cdot \rho_{p\_hat} \cdot g \cdot R^2}{9 \cdot \mu} \right)^2$$

843 Where  $V_0$  is either the seawater-density corrected velocity from Smayda or the  $dODdt$   
844 parameter we calculated above, and  $H$  is the one-hot binary scalar in  $[0,1]$  corresponding to  
845 whether the  $i$ 'th data point in our  $N$  observations was from Smayda's or our dataset,  
846 respectively. We used R's `optim()` function with the 'L-BFGS-B' method with initial parameters  
847 values of  $S = 0.03$  and  $\rho_{p\_hat} = 100$  and repeated this fit for 500 10-fold (10% out-of-bag)  
848 bootstrap samples of individual observations across our full dataset and Smayda's to gain an  
849 estimate of the error on the parameters.

850  $S$  and  $\rho_{p\_hat}$  fits were positively correlated across testing/training folds (Pearson's  $\rho = 0.97$ ),  
851 however mean values were fairly limited, with  $S = 0.028 \pm 0.002$  and  $\rho_{p\_hat} = 78 \pm 6.4 \text{ kg}\cdot\text{m}^{-3}$   
852 (with error equal to the standard deviation of estimates across 500 folds). These narrow  
853 estimates indicated that the fits were reasonably well-defined by the underlying dataset. The  
854 means and standard deviations across predictions of out-of-bag samples are what we have  
855 reported as means and standard error in Table 1 and propagated along with inter-replicate  
856 and batch error reported in the figures and text.

857

### 858 **Percentage of clumps measurements**

859 To measure percentage of clumps across all mutants and transfers in Figure 2 - figure  
860 supplement 1C, we first sonicated saturated *S. arctica* cultures using a Branson 450 Digital  
861 Sonifier (3 pulses of 15 sec, 10% amplitude). Cells were then diluted in fresh MB (1:250  
862 dilution) and cell concentration was then measured using a hemocytometer. Approximately 20  
863 cells were then transferred per well in a 96 well plate. Cells were then monitored every 24  
864 hours using an inverted optical microscope and the percentage of clumps observed after

865 cellularization was measured manually using a tally counter. This experiment was performed  
866 three independent times and error bars are standard deviations.

867

## 868 **Microscopy**

869 Microscopy of live and fixed cells was performed using a Zeiss Axio Observer Z.1  
870 Epifluorescence inverted microscope equipped with Colibri LED illumination system and an  
871 Axiocam 503 mono camera. An EC Plan-Neofluar 40x/0.75 air objective was used for images  
872 of fixed cells and an N-ACHROPLAN 20x/0.45na Ph2 air objective was used for all live  
873 imaging, unless indicated otherwise.

874

## 875 **Cell fixation and staining**

876 Throughout this study, saturated *Sphaeroforma* cultures were mildly sonicated prior to diluting  
877 them 250X in fresh marine broth to initiate a synchronized culture. To assess for any  
878 temperature dependency, cultures were grown at both 17°C and 12°C, and measurements  
879 were conducted every 12 hours for a duration of 72 hours. For every time-point, cells were  
880 fixed using 4% formaldehyde and 250mM sorbitol for 30 minutes before being washed twice  
881 with PBS. For nuclei staining cells were centrifuged at 1000 rpm for 3 min after fixation and  
882 washed again three times with PBS before adding DAPI at a final concentration of 5 µg/mL to  
883 5 µl of concentrated sample. DAPI-stained samples were imaged to measure DNA content  
884 and coenocyte size. It is important to note that results obtained from fast-settling mutants prior  
885 to cell release correspond to measurements of unicellular coenocytes (24 hours for 17°C and  
886 36 hours for 12°C), whereas results collected after cell release correspond to measurements  
887 of multi-celled clumps (48 hours for 17°C and 72 hours for 12°C). For cell wall staining, cells  
888 were incubated with Calcofluor-white (Sigma-Aldrich) at a final concentration of 5 µg/ml from  
889 a 200X stock solution prior to fixation. Cells were then fixed as previously mentioned and  
890 concentrated before being disposed between slide and coverslip.

891

## 892 **Live-cell imaging**

893 For live-cell imaging, saturated cultures were diluted 250x in fresh marine broth medium inside  
894 a µ-Slide 4 or 8 well slide (Ibidi) at time zero. To ensure oxygenation during the whole period  
895 of the experiment, the cover was removed. To maintain the temperature at 17 or 12°C we  
896 used a P-Lab Tek (Pecon GmbH) Heating/Cooling system connected to a Lauda Ecoline E100  
897 circulating water bath. To reduce light toxicity, we used a 495nm Long Pass Filter (FGL495M-  
898 ThorLabs). For plasma membrane live staining (Figure 3B, Video 3), FM4-64 (Invitrogen) at a  
899 final concentration of 10µM from a 100× DMSO diluted stock solution was added at time 0  
900 unless indicated otherwise in figure legends. For cytoplasmic staining of cells in Figure 3-

901 figure supplement 1, cells were either stained with CellTrace™ CFSE Cell Proliferation Kit  
902 (Thermofisher) or CellTrace™ Calcein Red-Orange (Thermofisher).

903

#### 904 **Image analysis**

905 Image analysis was done using ImageJ software (version 1.52) (Schneider et al., 2012). For  
906 nuclear content distribution across *Sphaeroforma sp.*'s life cycle, fixed and DAPI-stained  
907 coenocytes were imaged and the number of nuclei per coenocyte was counted using the  
908 ObjectJ plugin in imageJ. To compute nuclear duplication times,  $\log_2$  of geometric mean of  
909 DNA content was calculated as:  $\log_2(\text{geommean}) = \sum_i f_i * \log_2(x_i)$  where  $f_i$  is the fraction of  
910 cells and  $x_i$  the DNA content (ploidy) of each  $i$ -th DNA content bin. Nuclear doubling times  
911 were computed as linear regression of  $\log_2$  of geometric mean of DNA content versus time.  
912 Note that for *S. tapetis*, nuclear doubling times could not be computed due to the asynchrony  
913 in growth. For measurements of cell volume in live and fixed cells we used the oval selection  
914 tool to draw the contour of each cell and measured cell perimeter. As cells are spherical, we  
915 computed cell volume as:  $V = 4/3\pi r^3$  where  $r$  is the cell radius. For measurements of clumps  
916 perimeter, we transformed the images into binaries to ensure later segmentation. We then  
917 used the particle analysis function in ImageJ with a circularity parameter set to 0.15–1 to  
918 measure cell perimeter. For nuclear number-to-volume ratios, the number of nuclei was  
919 divided by the coenocyte volume measured as previously described for fixed cells. All Figures  
920 were assembled with Illustrator CC 2020 (Adobe). Several figures were generated using  
921 ggplot2 in R version 4.0.5 (Wickham, 2016).

922

#### 923 ***Sphaeroforma arctica* genome sequencing and assembly**

924 Genomic DNA was extracted for the ancestral strain (AN) and a single clonal isolate from each  
925 evolved population (S1-S10) using QIAamp DNA Blood Midi Kit (Qiagen) following the  
926 manufacturer's recommendations from 50 mL culture incubated at 17 °C for 5 days in 75 cm<sup>2</sup>  
927 flasks. The Qubit (*Invitrogen*) quantification ranged between 3 and 13 µg of genomic DNA in  
928 total. All of the subsequent steps were performed by the CRG Genomics Unit (Barcelona):  
929 sequencing libraries were prepared from the pure high molecular weight DNA using TruSeq  
930 DNA HT Library Preparation kit (*Illumina*® *HiSeq*® *Sequencing v4 Chemistry*). A paired-end  
931 library with a target insert size of ~500 bp was sequenced on an *Illumina*® HiSeq2500 platform  
932 in paired-end mode, with read lengths of 125 bp. The resulting paired raw read files were  
933 demultiplexed by the sequencing facility and data stored in two separate, gzip-compressed  
934 FASTQ files of equal sizes. Genome sequencing data has been deposited in NCBI SRA under  
935 the BioProject accession PRJNA693121.

936

## 937 **Bioinformatic analyses of the genomes**

938 Data processing. On average, each paired-end sequencing library contained ~58.8 million  
939 reads of 125 bp sequence-lengths (Figure 4-Source Data 1), equalling ~7.35 billion base-pairs  
940 (Gbp). From these data, we carefully removed adapter sequences and reads shorter than 50  
941 bp from the raw read data using *trimmomatic* v0.36 (Bolger et al. 2014), yielding an average  
942 of ~4.36 Gbp of filtered sequence data per genome (Figure 4-Source Data 1). The quality of  
943 both raw and trimmed sequencing data was assessed in FastQC v0.11.7 (Andrews, 2010). In  
944 more detail, based on the FastQC output for raw reads, we initiated trimming by calling the  
945 following parameters:

946 *ILLUMINACLIP:Nextera+TruSeq3-PE2.fa:3:25:10 CROP:110 LEADING:30 TRAILING:25*  
947 *SLIDINGWINDOW:4:28 MINLEN:50*

948 This translates into the following trimming steps:

- 949 • cut adapters and other *Illumina* specific sequences using a combined file of default  
950 adapters (“Nextera.fa” AND “TruSeq3-PE2.fa”) to catch as many spurious  
951 contaminations during library prep as possible, with seed mismatches = 3; palindrome  
952 clip threshold = 25; simple clip threshold = 10;
- 953 • end-clipping of the final 15bp of all reads, due to evidence for elevated adapter content;
- 954 • quality-clip all bases on leading ends as long as bases were of lower quality than Q <  
955 30;
- 956 • removing all bases on trailing ends as long as bases were of lower quality than Q <  
957 25; and,
- 958 • finally, conducting a sliding window approach, where the reads were trimmed once the  
959 average quality within a window of four consecutive bases falls below a threshold of Q  
960 <28.

961

962 The trimming output consisted of four FASTQ files for each genome, of which two files  
963 contained intact paired-end reads, and another two files containing all unpaired reads for each  
964 end separately.

965 Repeat-masking of reference genome. We relied on the latest (i.e., fourth) assembly version  
966 of the *S. arctica* reference genome (Sarc4; (Dudin et al., 2019)) for variant detection and  
967 annotation. Initial runs of the read-mapping steps revealed a high proportion of clustered  
968 variants (~20.4%) concentrated in certain regions of the genome (Figure 4-Source Data 2).  
969 We investigated this phenomenon and determined that the issue was caused by repetitive  
970 stretches of sequence and thus decided to mask all of the potentially problematic repeat  
971 regions. For this, repetitive regions were screened for and properly annotated in  
972 *RepeatMasker* v4.1.1 (Smit et al., 2015) relying on the 20181026 release of *GIRI RepBase*

973 database for annotations (Bao et al., 2015) and applying the slow high-sensitivity search mode  
974 with the following parameters: *-pa 10 -s -gff -excln -species Opisthokonta*.

975 Variant prediction. We performed read alignment, variant calling, variant filtering in CLC  
976 Genomic Workbench v20.0.4 (©Qiagen) and our analytical pipeline was structured into the  
977 following steps:

- 978 • Read alignment. Paired-end reads were merged (assuming insert lengths between 400  
979 and 600bp), and both paired and unpaired reads were aligned against the reference  
980 genome (with settings: Length fraction  $\geq 0.9$ ; Similarity fraction  $\geq 0.9$ ; Match score = 1;  
981 Mismatch cost = 3; Insertion/Deletion Open Cost = 5; Insertion/Deletion extend cost = 3;  
982 Global Alignment = no). Finally, reads were deduplicated (maximum representation of  
983 minority sequence = 0.2).
- 984 • Variant calling. We called variants using CLC's "Fixed Ploidy Variant Detection"  
985 assuming a haploid genome (Ploidy = 1) for *Sphaeroforma arctica*. We further required  
986 a variant probability of at least 90%, ignoring positions in excess of 90x coverage,  
987 broken read pairs and non-specific matches. All variants needed to be covered by at  
988 least 10 variant-bearing reads, and a minimum consensus of 80% (i.e., at least 10/12  
989 variant supporting reads). We also applied the following read quality filters:  
990 neighborhood radius = 10; minimum central quality = 20; minimum neighborhood  
991 quality = 20), and read direction filters (direction frequency = 0.05; relative read  
992 direction filter = yes (significance = 0.05); read position filter = yes (significance = 0.05).
- 993 • Variant filtering. 1) To consider only variants that have emerged through the course of  
994 evolution, we automatically removed mutations present in the ancestor (AN). 2) We  
995 then went on to manually curate all mutation predictions. We did this by aligning the  
996 mapping tracks (profiles) of all re-sequenced genomes (AN, S1 – S10) and screening  
997 all initial candidate mutations. The overwhelming majority of \*mutations\* were visually  
998 shared across all evolved clones but not called universally due to extremely low  
999 statistical support, or low local coverage in some of the genomes. The final dataset  
1000 hence only contained 25 predicted variants, and exported these for each of the ten  
1001 evolved single clones as Variant Call File (VCF) format.
- 1002 • Variant annotation. We annotated filtered variants from converted VCF files with  
1003 *breseq v0.33.2* (Deatherage & Barrick, 2014). More specifically, we converted VCF  
1004 files into *breseq*'s Genome Diff (GD) file format using the command "*gdtools VCF2GD*".  
1005 We then annotated all genomes in GD format jointly by running the command "*gdtools*  
1006 *ANNOTATE*" and specifying original *S. arctica* genome assembly (Sarc4) in  
1007 GenBankFormat (GBK) as reference. Mutations were tabulated and sorted. Finally, we  
1008 counted and categorized both observed mutations and non-synonymous and

1009           synonymous sites at risk across the reference genome using the command “*gdtools*  
1010           *COUNT -b*”.  
1011

1012 **Figure legends**

1013

1014 **Figure 1. Sedimentation dynamics of *Sphaeroforma arctica* coenocytes during the life**  
1015 **cycle**

1016 (A) Cladogram representing the position of ichthyosporeans including *Sphaeroforma* species  
1017 within the eukaryotic tree.

1018 (B) Schematic representation of the coenocytic life cycle of *S. arctica*.

1019 (C) Figure adapted from Figure 1 (SMAYDA & J., 1970) (grey points) was used to scale  
1020 velocity measurements determined in our sedimentation assay to physical ( $\mu\text{m/s}$ ) units  
1021 (red points) (Methods). Error bars represent the 95% CI for each unique genotype,  
1022 timepoint, and temperature measurement presented in our study (N=3 for each of 1 or 2  
1023 independent replications). Values were log-transformed prior to calculation of error. This  
1024 figure is to illustrate where our data fit in the scheme of known plankton sedimentation  
1025 rates. For our best estimations of cellular density and velocity in meters per second, a  
1026 subset of this data from Smayda's Appendix Table 1 was used (Methods).

1027 (D) Using the Smayda dataset as a calibrating reference, we used measurements of  
1028 sedimentation rate using our assay along with cellular perimeter measurements to calculate  
1029 maximum likelihood estimates of cellular density. See Methods and Figure 1 – Source Data.  
1030 These estimates are plotted on a landscape illustrating the relationship between density and  
1031 size on sedimentation rate (grey contour lines).

1032 (E) Sedimentation rates of *Sphaeroforma* during the life cycle at 17°C. Every trace represents  
1033 an independent experiment.

1034 (F) Distributions of nuclear content of *S. arctica* cells during the life cycle at 17°C, measured  
1035 by microscopy (n > 500 cells/timepoint).

1036 (G) Quantification of mean DNA content per time point (expressed as log2 of geometric mean)  
1037 for cells grown in marine broth at 17°C (n > 500 cells/timepoint).

1038 (H) Average coenocyte volume per timepoint at 17°C (n = 100 coenocyte/timepoint).

1039 (I) Sedimentation rates of *S. arctica* coenocytes during the life cycle at 17°C.

1040

1041 **Figure 1 – Source Data 1. Our data used for estimating sedimentation rate in metric**  
1042 **units and density in mass per volume.**

1043 'V\_au' is sedimentation rate in AU OD600 units per second.

1044 'R\_meters' is the mean radius of cells for the genotype and environment

1045 'Species', genotype, temp, hours\_growth are information for aggregating the data based on  
1046 genotype and environment.



1047 'V\_mu' is the maximum likelihood estimate of cellular sedimentation rate - the mean of all out-  
1048 of-bag samples used in fitting - in meters per second.

1049 'V\_se' is the standard deviation of cellular sedimentation rate across all out-of-bag samples in  
1050 the fitting.

1051 'pp\_mu' the maximum likelihood estimate of density - the mean of all out-of-bag samples used  
1052 in fitting - in kg/m<sup>3</sup>.

1053 'pp\_se' the maximum likelihood estimate of density - the standard deviation of all out-of-bag  
1054 samples used in fitting - in kg/m<sup>3</sup>.

1055

1056 **Figure 1 – Source Data 2. Smayda dataset used for calibrating our dataset. Adapted**  
1057 **from (SMAYDA & J., 1970) Appendix Table 1**

1058 'classification', species are from his table annotation.

1059 'salt\_percent' is the percent salt reported in the table.

1060 'V\_meters\_per\_second' is the velocity reported, converted from meters per day to meters per  
1061 second.

1062 'Pf' is the density of the media based on the reported temperature and salt concentration,  
1063 estimated by the data from Millero and Huang.

1064 'R\_meters' is the mean radius in meters. When a range was given, this is the average of that  
1065 range.

1066 'Pp\_' is the density of the sample

1067 'Pp' is the excess density

1068 'V\_exp' is the expected velocity in the seawater used in our experiments (37.4 g/l)

1069

1070 **Figure 1 – Source Data 3. The Millero and Huang data (Millero & Huang, 2009) used for**  
1071 **estimating seawater density based on salinity and temperature.**

1072 'temp\_C' temperature in degrees Celsius

1073 'salinity' salt in g/l

1074 'density\_kgm3' excess density in kg m<sup>-3</sup>

1075 'density' density in kg m<sup>-3</sup>

1076

1077 **Figure 2. Rapid evolution of fast-settling and clumpy mutants**

1078 (A) Schematic representation of the experimental evolution design using sedimentation as a  
1079 selective pressure. All 10 replicate populations (S1-S10) were isolated from the same  
1080 ancestral culture (AN) and were subject to 56 transfers over 8 weeks of selection.

1081 (B) Representative images of the ancestral culture (AN) and three evolved mutants (S1, S5,  
1082 S6) with varying clumping capability after 5 days of growth. Bar, 50µm.

1083 (C) Sedimentation rates of *S. arctica* evolved populations per number of transfers shows rapid  
1084 emergence of fast-settling phenotypes, particularly in S1.

1085 (D) Sedimentation rates of single clones of *S. arctica* evolved mutants after 56 rounds of  
1086 selection displays three distinct settling phenotypes (Slow, Intermediate and Fast). Associated  
1087 with Video 1.

1088 (E) Clump size distribution of evolved clones (expressed as log<sub>10</sub> of perimeter) shows that  
1089 fast-settling mutants (S1, S4, S9) show bigger clump size (n > 800 measurements/timepoint).  
1090

1091 **Figure 2- figure supplement 1. Clump size of evolved mutants correlates with increased**  
1092 **number of cells per clump**

1093 (A) Approximation of the constant population size derived from nuclear doublings over the  
1094 course of 48 hours. Nuclei numbers were estimated from total cell number and average  
1095 number of nuclei per cells (after cell-sorting). At 24 hours, a constant fraction of cells has been  
1096 transferred to fresh medium, which induces a bottleneck.

1097 (B) Sedimentation rates of S1 clumps after incubation for 2hours in different media or after  
1098 sonication. MB= Marine Broth, ASW = Artificial sea water (Salt concentration = 36.4 g/L), 2X  
1099 (Salts concentration = 72.8g/L), 0.5X (Salts concentration = 18.2g/L), PBS = Phosphate  
1100 Buffered Saline 1X, Proteinase K 200 µg/mL and sonication (3 pulses of 15 sec, 10%  
1101 amplitude). Representative images on the right show the dissociation of S1 clumps after  
1102 sonication. Bar, 50µm.

1103 (C) Percentage of clumps formed after 72h of all evolved mutants per number of transfers (n  
1104 > 200 coenocytes at cell-release/strain). Example images on the left of detached or clumpy  
1105 cells after cell-release. Bar, 50µm.

1106 (D) Number of cells per clump in all evolved mutants (expressed as log<sub>10</sub> of perimeter)  
1107 illustrates the linear correlation between sedimentation rate and number of cells per clump. (n  
1108 = 13 clumps for AN and 50 clumps for all evolved mutants of at least 5 attached cells together).

1109 (E) Linear correlation between clump size of the fast-settling mutants (S1, S4, S9) and number  
1110 of cells per clump compared to the ancestral strain (AN).

1111

1112 **Figure 3. Clumps are formed by incomplete cell-cell separation in fast-settling mutants.**

1113 (A) Time-lapse images of the life cycle of *S. arctica* ancestral strain (AN) and the fast-settling  
1114 mutants (S1, S4, S9) at 12°C, show that clumps are observed concomitantly with release of  
1115 new-born cells. Associated with Video 2. Bar, 50 µm

1116 (B) Plasma membrane staining using FM4-64 show that plasma membrane invaginations  
1117 during cellularization seems to occur normally in fast-settling mutants. Associated with Video  
1118 3. Bar, 50µm.

1119 (C) Cell-wall staining using calcofluor-white indicate cells are still separated by a cell-wall  
1120 inside fast-settling clumps, suggesting that clumps are formed post-flip. Bar, 50µm.

1121 (D) Number of cells detaching per clumps at cell release and for the following 3 hours,  
1122 measured from time-lapse movies (n = 50 coenocytes at cell-release/strain).

1123 (E) Coenocyte volume at flip, measured from time-lapse movies, show that S4 and S9 are  
1124 significantly smaller when compared to AN and S1 (n = 50 coenocytes at flip/strain).

1125

1126

1127 **Figure 3- figure supplement 1. Fast-settling mutants cannot form clumps by**  
1128 **aggregation and show discreet differences in life-stages duration.**

1129 (A) Cell-wall staining show presence of a separating cell wall between individual cells in the  
1130 clumps of all fast-settling mutants. Bar, 50µm.

1131 (B) Experimental design and measurements of S1 clump formation by aggregation. AN and S1  
1132 cells are separated by sonication and stained with different cellular dyes prior to being mixed  
1133 together for a complete life cycle of 72 hours. Clumps of each separate or mixed colours are  
1134 then counted by microscopy. Circles represent the number of clumps observed in each  
1135 condition (more than 5 cells attached together). We show that when S1 is mixed with either  
1136 AN or itself (1:1 ratio) it mostly forms mono-coloured clumps. Representative images of mono-  
1137 coloured clumps. Bar, 50 µm

1138 (C) Mean coenocyte perimeter over time (10 cell traces per strain) at 12°C, aligned to time 0,  
1139 reveals discreet differences in coenocyte perimeter and life-cell stages among fast-settling  
1140 mutants. Orange squares represents the flip timepoint in each trace.

1141 (D) Duration of growth, cellularization and post-flip represented as box-plots at 12°C (n > 28  
1142 coenocytes each).

1143

1144 **Figure 4. Sedimentation rates variation in fast-settling mutants is associated with**  
1145 **variations in cell size and cellular density.**

1146 (A) Sedimentation rates of *S. arctica* AN and evolved mutants during the life cycle at 17°C.  
1147 Every trace represents an independent experiment.

1148 (B) Average perimeter measured from fixed cells every 12h over a complete life cycle of 72  
1149 hours at 17°C shows that fast-settling mutants increase their size upon-cell release. Every  
1150 trace represents an independent experiment (n > 180 measurements/timepoint for each  
1151 independent experiment).

1152 (C) Average perimeter of fast-settling cells and clumps at 24 hours and 60 hours respectively  
1153 show that S4 and S9 cells and clumps have a smaller size when compared to S1. Every  
1154 square represents an independent experiment, and the white circle represents the median (n  
1155 > 180 coenocytes/timepoint for each independent experiment).

1156 (D) Sedimentation rates of fast-settling individual coenocytes (before cellularization) and  
1157 clumps (after cell-release) at 24 hours and 60 hours respectively show that S4 and S9 single  
1158 cells sediment faster when compared to S1 and AN. Every square represents an independent  
1159 experiment, and the white circle represents the median.

1160 (E) Quantification of mean DNA content per time point (expressed as log<sub>2</sub> of geometric mean)  
1161 for fast-settling mutants grown in marine broth at 17°C. Every trace represents an independent  
1162 experiment (n > 400 coenocytes/timepoint for each independent experiment).

1163 (F) Nuclear doubling time, calculated by linear regression of mean nuclear content at  
1164 timepoints from 0 hr to 24 hours. Every square represents an independent experiment, and  
1165 the white circle represents the median (n > 400 coenocytes/timepoint for each independent  
1166 experiment).

1167 (G) Boxplots of cell volume measurements of DAPI-stained fixed cells. For 1-, 4-, 16-, and 64-  
1168 nuclei cells. Cells with 1 nucleus represent new-born cells at the end of the experiment (n >  
1169 80 coenocytes/DNA content).

1170 (H) Boxplots of nuclear number-to-volume ratio of DAPI stained cells show significant increase  
1171 for S4 and S9 fast-settling mutants. Every square represents an independent experiment, and  
1172 the white circle represents the median (n > 600 coenocytes/strain).

1173 (I-K) Temporal transcript abundance of genes mutated in fast-settling phenotype across the  
1174 native life cycle of *S. arctica*.

1175

1176

1177 **Figure 4- figure supplement 1. Increased sedimentation rates in fast-settling mutants is**  
1178 **independent of temperature**

1179 (A) Sedimentation rates of *S. arctica* AN and evolved mutants during the life cycle at 12°C.  
1180 Every trace represents an independent experiment.

1181 (B) Average perimeter measured from fixed cells every 12h over a complete life cycle of 72  
1182 hours at 12°C shows that fast-settling mutant increase their size upon-cell release. Every trace  
1183 represents an independent experiment (n > 130 measurements/timepoint for each  
1184 independent experiment).

1185 (C) Average perimeter of fast-settling cells and clumps at 36 hours and 72 hours respectively  
1186 show that S4 and S9 single cells and clumps have a smaller size when compared to S1 at  
1187 12°C. Every square represents an independent experiment, and the white circle represents  
1188 the median.

1189 (D) Sedimentation rates of fast-settling mutants (before cellularization) and clumps (after  
1190 cellularization) at 36 hours and 72 hours. Every square represents an independent  
1191 experiment, and the white circle represents the median.

1192 (E) Distributions of nuclear content of *S. arctica* AN and fast-settling mutants during the life  
1193 cycle at 17°C measured by microscopy of DAPI-fixed cells (n > 400 coenocytes /timepoint).

1194 (F) Distributions of nuclear content of *S. arctica* AN and fast-settling mutants during the life  
1195 cycle at 12°C measured by microscopy of DAPI-fixed cells (n > 420 coenocytes/timepoint for  
1196 each independent experiment).

1197 (G) Quantification of mean DNA content per time point (expressed as log<sub>2</sub> of geometric mean)  
1198 for fast-settling mutants grown in marine broth at 12°C. Every trace represents an independent  
1199 experiment (n > 420 coenocytes/timepoint for each independent experiment)

1200 (H) Nuclear doubling time, calculated by linear regression of mean nuclear content at time  
1201 points from 0 hours to 24 hours at 12°C. Every square represents an independent experiment,  
1202 and the white circle represents the median (n > 420 coenocytes/timepoint for each  
1203 independent experiment).

1204 (I) Boxplots of cell volume measurements of DAPI-stained fixed cells at 12°C. For 1-, 4-, 16-,  
1205 and 64-nuclei cells. Cells with 1 nucleus represent new-born cells at the end of the experiment  
1206 (n > 50 coenocytes/DNA content).

1207 (J) Boxplots of nuclear number-to-volume ratio of DAPI stained cells at 12°C. Every square  
1208 represents an independent experiment, and the white circle represents the median (n > 300  
1209 coenocytes/strain).

1210 (K) Temporal transcript abundance of genes mutated in intermediate and slow-settling  
1211 phenotypes across the native life cycle of *S. arctica*.

1212

1213 **Figure 5. Sedimentation rate variations across *Sphaeroforma* species is associated**  
1214 **with clumping and increased nuclear number-to-volume ratio.**

1215 (A) A cladogram representing the position of all *Sphaeroforma* sister species used in the study.

1216 (B) Representative images of different *Sphaeroforma* sp. at cell release. Arrowheads indicate  
1217 the formation of clumps. Associated with Video 4. Bar, 50µm.

1218 (C) Number of cells detaching at cell release, measured from time-lapse movies, show  
1219 significant differences among the different sister species. (n > 48 coenocytes/*Sphaeroforma*  
1220 sp.).

1221 (D) Sedimentation rates of *Sphaeroforma* sp. cells (before cellularization) and clumps (after  
1222 cell release) at 36 hours and 72 hours respectively. Every square represents an independent  
1223 experiment, and the white circle represents the median.

1224 (E) Quantification of mean DNA content per time point (expressed as log<sub>2</sub> of geometric mean)  
1225 for *Sphaeroforma* sp. grown in marine broth at 17°C. Every trace represents an independent  
1226 experiment (n > 300 coenocytes/timepoint for each independent experiment).

1227 (F) Nuclear doubling time, calculated by linear regression of mean nuclear content at time  
1228 points from 0 hr to 24 hours at 17°C. Every square represents an independent experiment,

1229 and the white circle represents the median. ( $n > 300$  coenocytes/timepoint for each  
1230 independent experiment)

1231 (G) Boxplots of nuclear number-to-volume ratio of DAPI stained cells at 17°C for  
1232 *Sphaeroforma* sister species. Every square represents an independent experiment, and the  
1233 white circle represents the median. ( $n > 300$  coenocytes/strain).

1234

1235 **Figure 5- figure supplement 1. *Sphaeroforma* sister species are distinct in growth,  
1236 sedimentation rates and cell volume.**

1237 (A Distributions of nuclear content of *Sphaeroforma* sister during the life cycle at 17°C of DAPI-  
1238 fixed cells measured by microscopy. Note that *S. tapetis* is asynchronous compared to all  
1239 other species ( $n > 300$  coenocytes per timepoint for each independent experiment).

1240 (B) Average perimeter measured from fixed cells every 12 hours over a complete life cycle of  
1241 72 hours at 17°C of *Sphaeroforma* sp. Every trace represents an independent experiment ( $n$   
1242  $> 140$  measurements per timepoint for each independent experiment).

1243 (C) Average perimeter of *Sphaeroforma* sp. cells and clumps at 0, 24, and 48 hours,  
1244 respectively, show that *S. gastrica*, *S. nootakensis*, *S. napiecek* and *S. sirkka* are smaller in  
1245 size at 17°C. Every square represents an independent experiment, and the white circle  
1246 represents the median ( $n > 140$  measurements/timepoint for each independent experiment).

1247 (D) Coenocyte volume at flip, measured from time-lapse movies, show that all *Sphaeroforma*  
1248 species apart from *S. arctica* have significantly smaller coenocyte volume at flip ( $n > 50$   
1249 coenocytes/strain).

1250 (E) Boxplots of cell volume measurements of DAPI-stained fixed *Sphaeroforma* sp.  
1251 coenocytes at 17°C. For 1-, 4-, 16-, and 64-nuclei cells. Cells with 1 nucleus represent new-  
1252 born cells at the end of the experiment. ( $n > 50$  coenocytes/DNA content).

1253

1254 **Video 1. Video of *Sphaeroforma arctica* AN and fast-settling (S1, S4, S9) cultures  
1255 sedimenting, obtained with a mobile phone (Samsung A20).**

1256 Time interval between frames is 0.5 sec. The movie is played at 7fps. We can observe rapid  
1257 cell sedimentation in S1, S4 and S9 when compared to AN. Note that S1 clumps are bigger  
1258 and sediment faster than the two other mutants. The movie was acquired for cultures pre-  
1259 grown for 72 hours at 12°C.

1260

1261 **Video 2. Time lapse of synchronized cells of *S. arctica* AN and fast-settling mutants (S1,  
1262 S4, S9).**

1263 Time interval between frames is 30 min. The movie is played at 7fps. Four distinct cells can  
1264 be seen undergoing a full life cycle at 12°C with the release of detached new-born cells for  
1265 AN or clumps for the mutants. Bar, 50  $\mu$ m.

1266

1267 **Video 3 Time lapse of cells of *S. arctica* AN and fast-settling mutants (S1, S4, S9)**  
1268 **stained with the membrane dye Fm4-64 obtained with epifluorescent microscopy.**

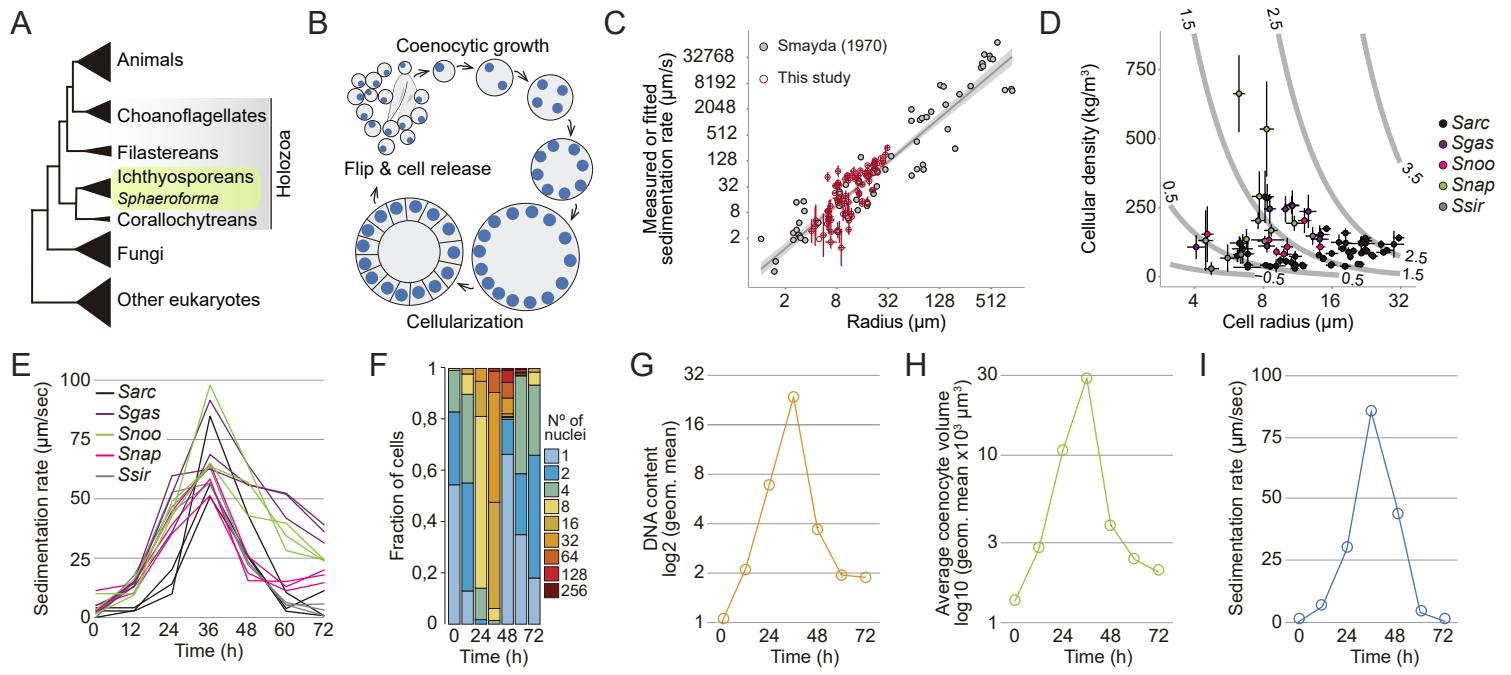
1269 Time interval between frames is 15 min. The movie is played at 7fps. Clumps can be seen  
1270 being formed after plasma membrane invaginations followed by cell release. Bar, 50  $\mu\text{m}$ .

1271

1272 **Video 4. Time lapse of 6 different *Sphaeroforma* species undergoing a complete life**  
1273 **cycle.**

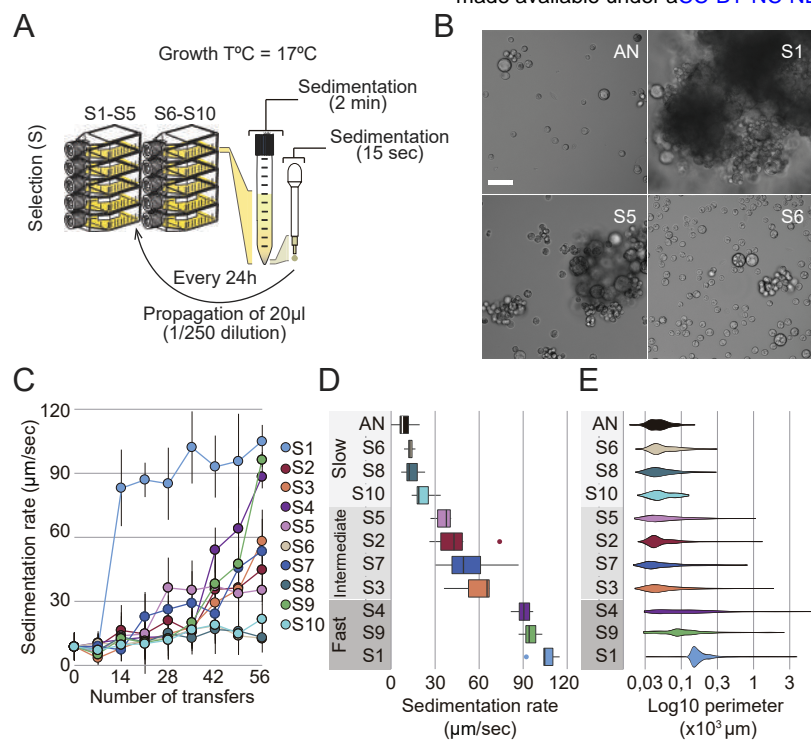
1274 Time interval between frames is 30 min. The movie is played at 7fps. Note the asynchrony of  
1275 *S. tapetis*, the capacity to clump of *S. gastrica* and *S. nootakensis*, and the small cell size of  
1276 all *Sphaeroforma* species compared to *S. arctica*. Bar, 50  $\mu\text{m}$ .

Figure 1





**Figure 2**



## Figure 2 - figure supplement 1

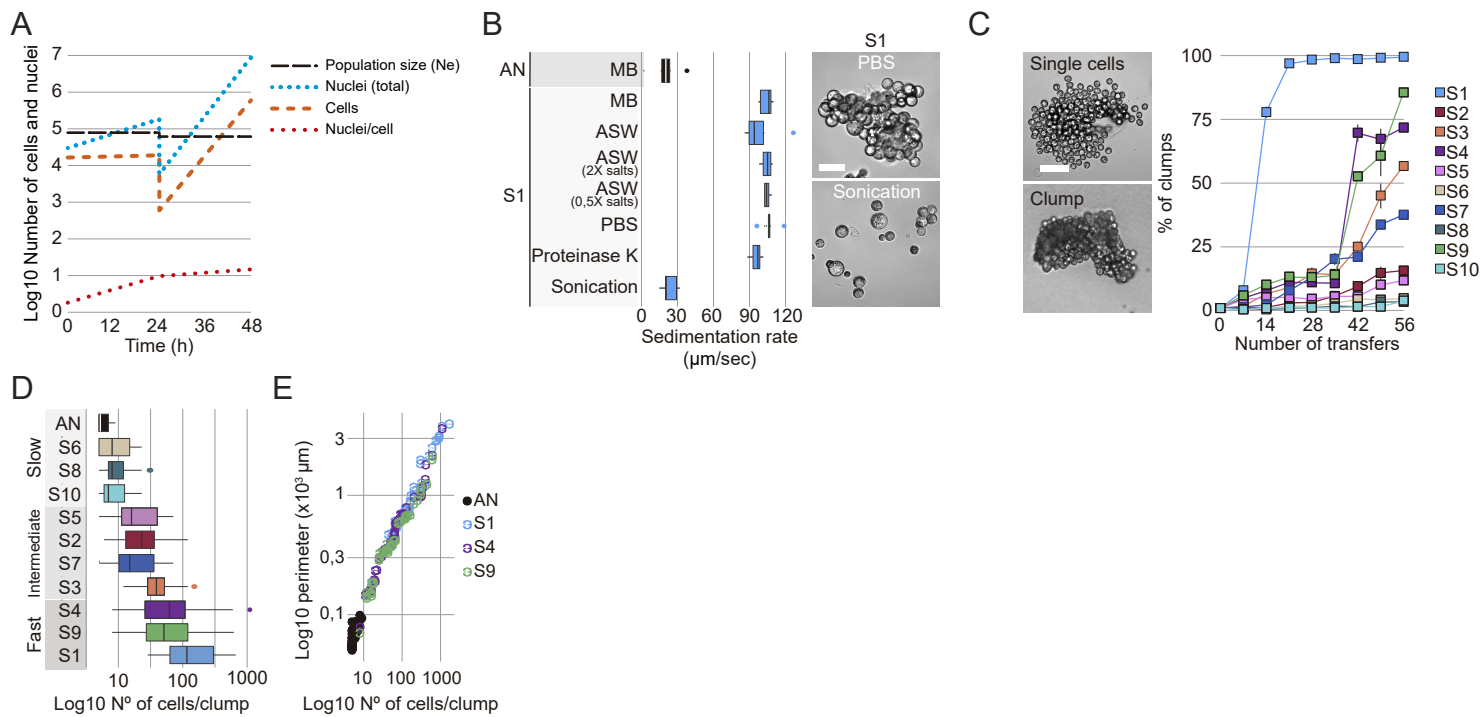


**Figure 3**

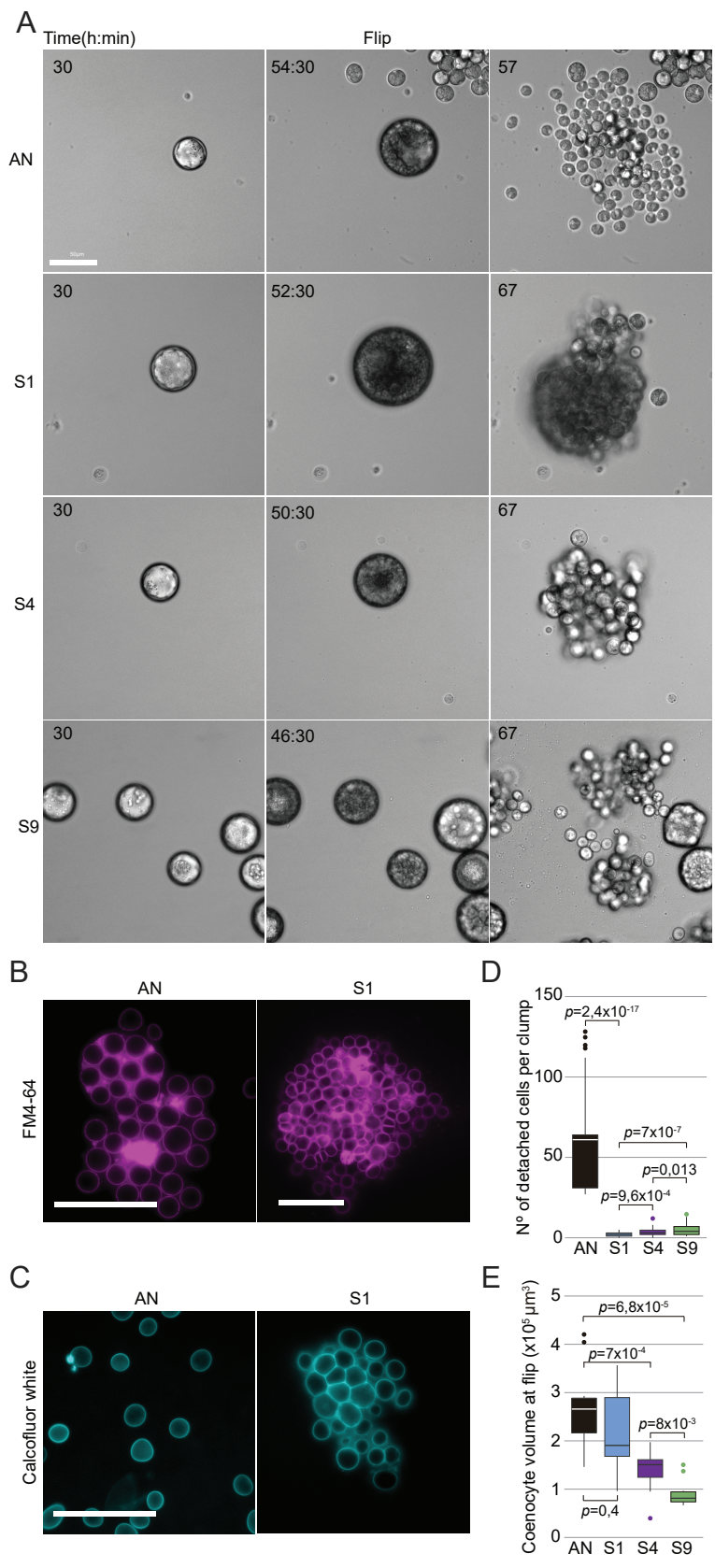


Figure 3 - figure supplement 1

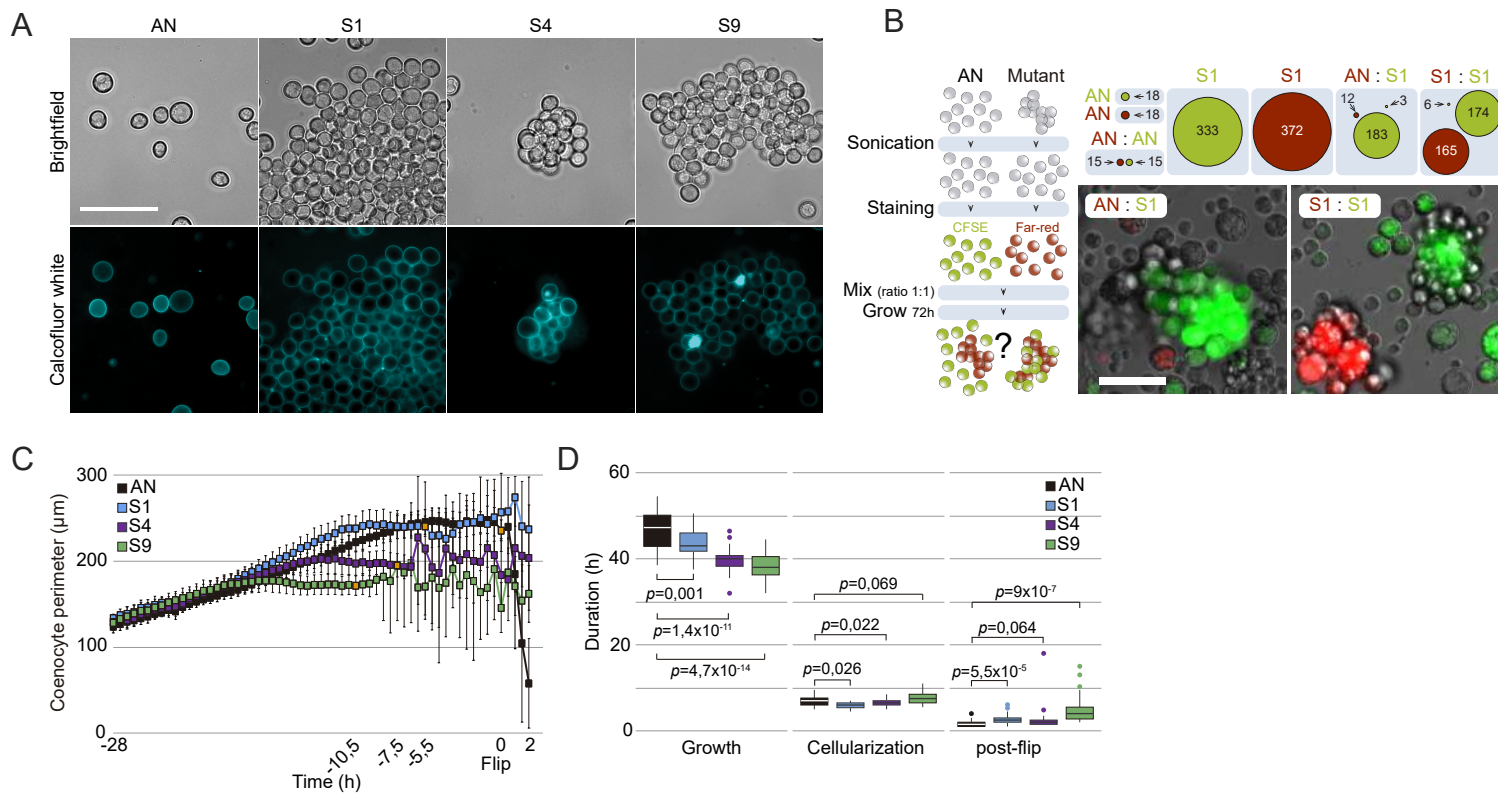


Figure 4

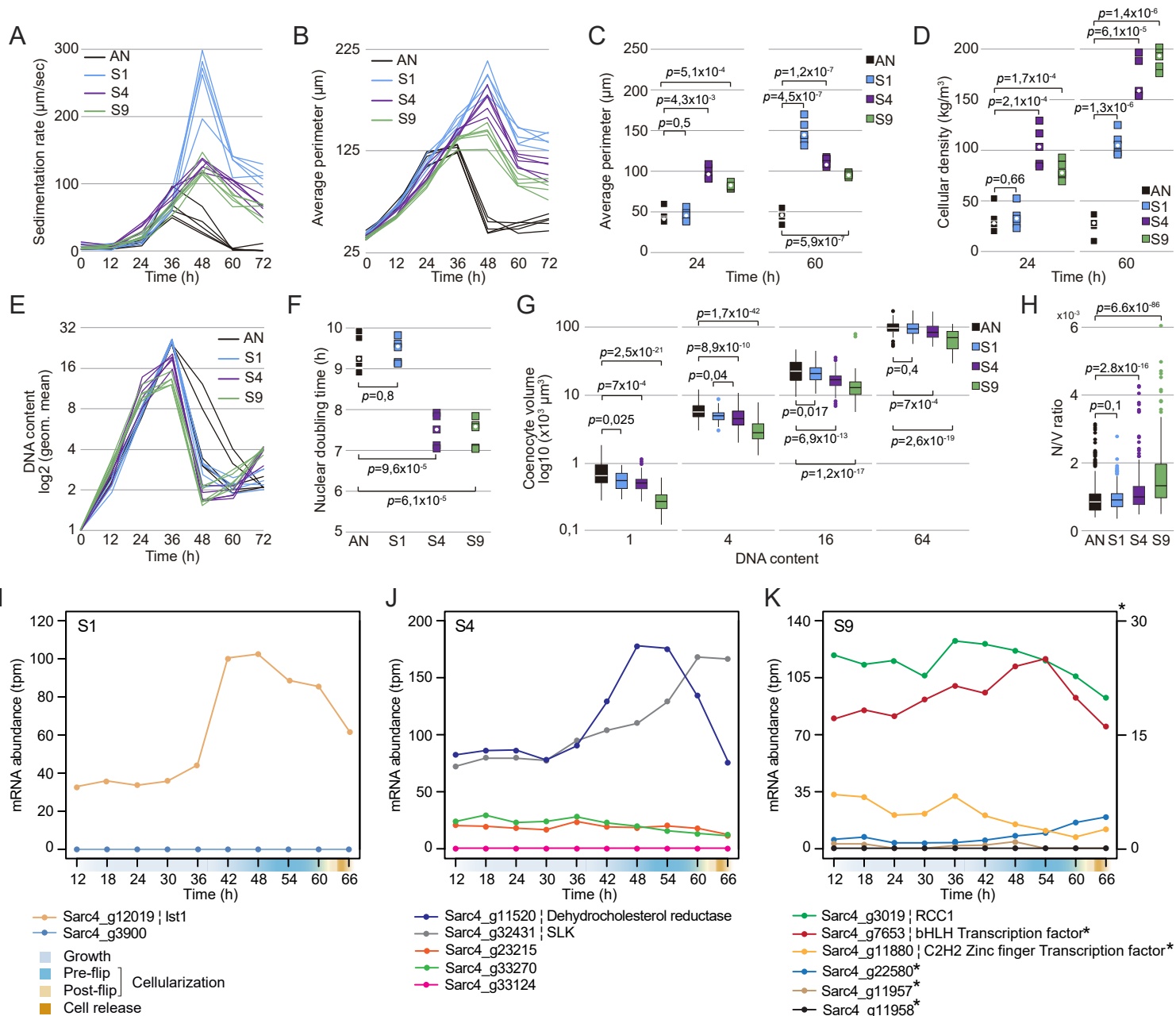
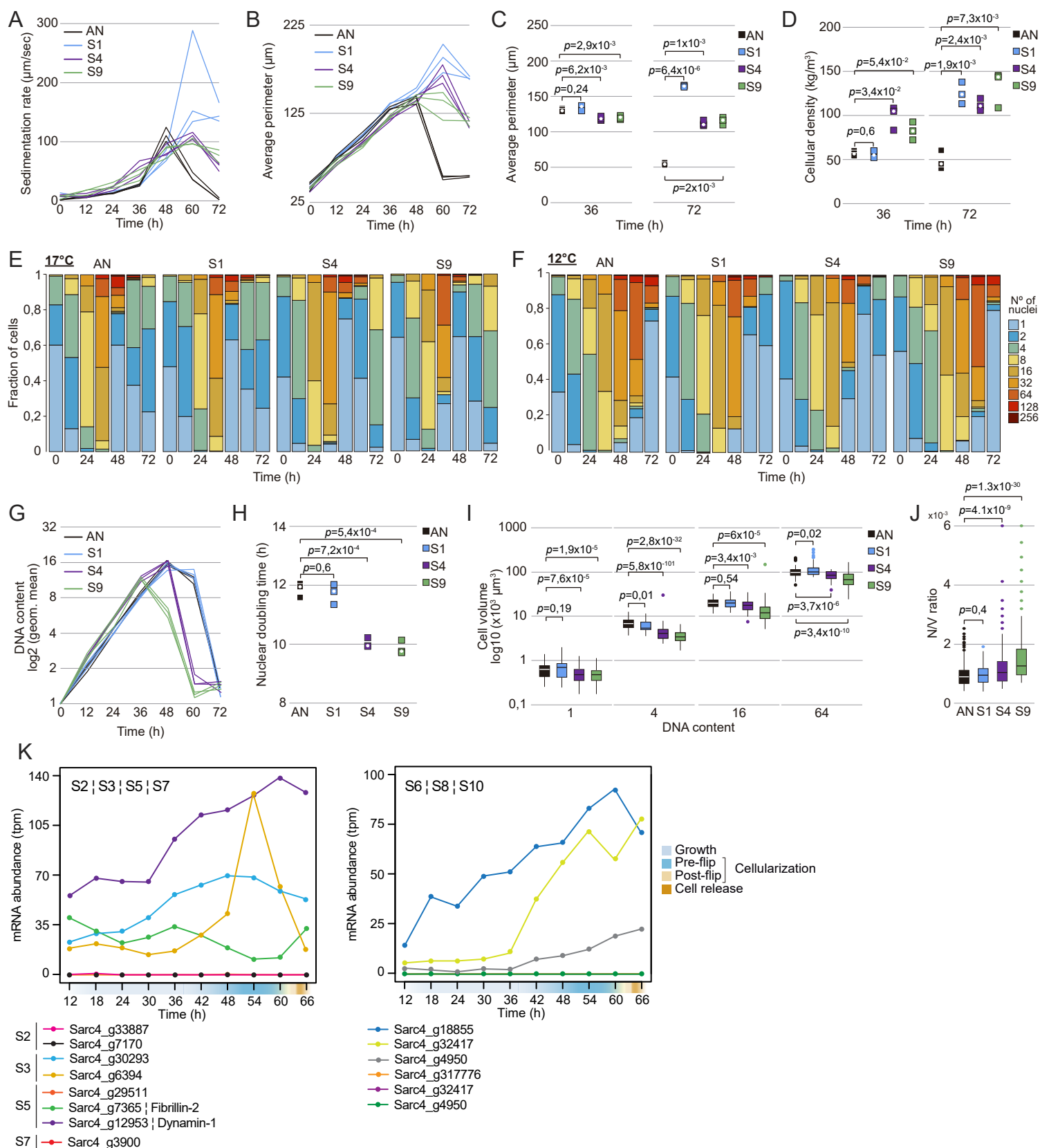


Figure 4 - figure supplement 1



## Figure 5

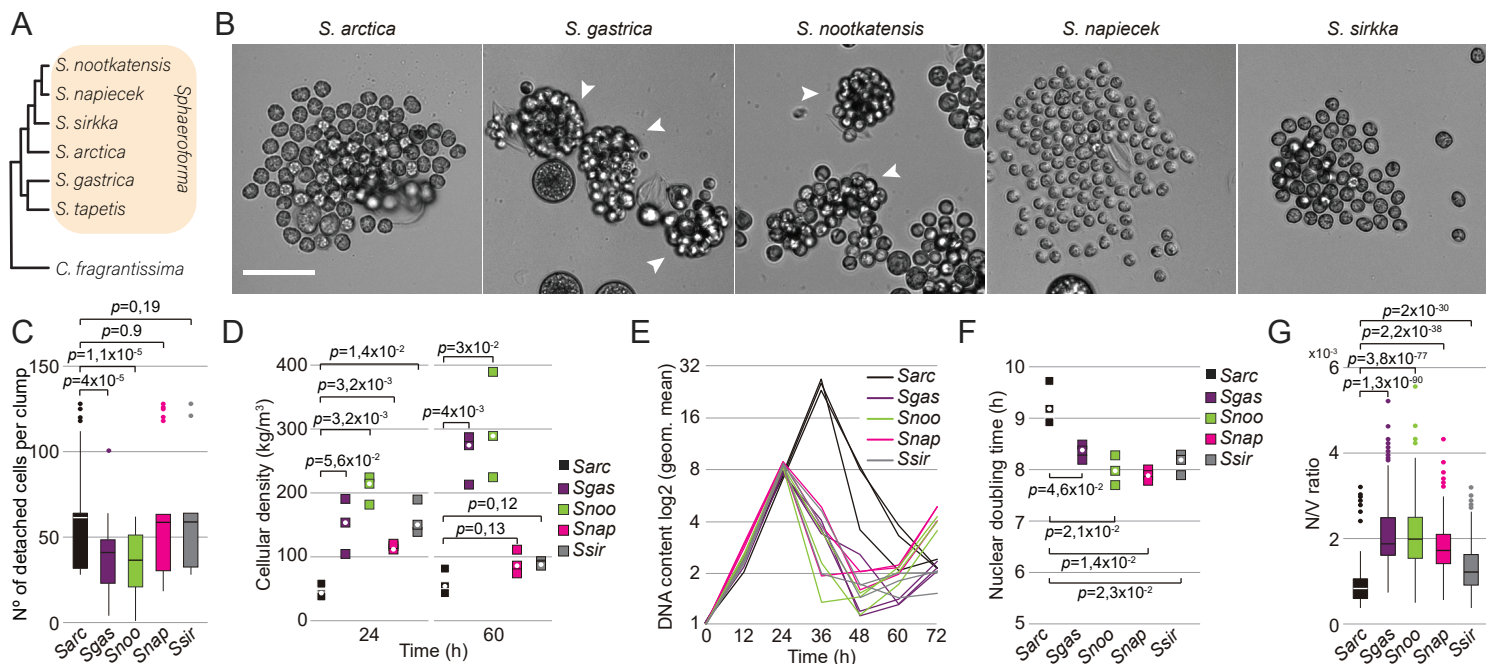


Figure 5 - figure supplement 1

